Performance of muon range detector for neutrino-nucleus interaction cross section measurements
（ニュートリノー原子核反応断面積測定のための ミューオン飛跡検出器の性能）

理学研究科

数物系専攻

久木田 直哉

Abstract

For precise measurement of neutrino oscillation, understanding of neutrino interactions on nucleus is indispensable. One of the main systematic errors in neutrino oscillation analysis in the T2K experiment is due to the difference in the acceptance and target materials between Super-Kamiokande and the near detector. In order to reduce this uncertainty, a new experiment, named WAGASCI, at the neutrino beamline in Japan Proton Accelerator Research Complex (J-PARC) has been proposed. Its main goals are measurements of cross section ratio of water to hydrocarbon and differential cross section of water and hydrocarbon with large acceptance.

In order to select neutrino charged current interaction except background generated out of target detector and reconstruct the momentum of muon generated from neutrino interaction, two muon range detectors, named SideMRDs, are planed to be installed next to the WAGASCI detector.

SideMRD consists of 11 iron plates and 10 scintillator layers. A scintillator layer is including 8 scintillators. For 2 SideMRDs, total 160 scintillators are required and the performance of scintillators were measured.

For SideMRDs, 320 multi-pixel photon counters (MPPC), produced by Hamamatsu Photonics, are used. To read out the MPPCs, the electronics based on SPIROC2D has been developed. The performance of the electronics is tested. The performance of SideMRDs is also tested after construction and transportation to J-PARC.

Contents

1 Introdection

1.1 Neutrino oscillation

Neutrino is one of the neutral elementary particles with spin 1/2 and interacts only through the weak interaction. Neutrino is classified into three types as flavors: electron neutrino(ν_e), mu neutrino(ν_μ), tau neutrino(ν_τ) and their anti-particles($\bar{\nu}_e, \bar{\nu}_\mu, \bar{\nu}_\tau$).

The standard model of elementary particle physics assumed the masses of the neutrinos were exactly zero and lepton flavor was conserved. The discovery of neutrino oscillation in atmospheric neutrinos by Super-Kamiokande[1] denied the assumption however because the existence of neutrino oscillation requires non-zero masses of neutrinos.

The neutrino flavor eigenstates of weak interaction, $|\nu_\alpha\rangle\,(\alpha = e, \mu, \tau)$, are described as the superposition of the neutrino mass eigenstates, $|\nu_i\rangle\,(i = 1, 2, 3)$. The mixing of mass eigenstates is given by an unitary matrix called the Pontecorvo-Maki-Nakagawa-Sakata (PMNS) matrix[2] as following:

$$|\nu_\alpha\rangle = \sum_i U_{\alpha i}\,|\nu_i\rangle\,. \tag{1.1}$$

The PMNS matrix is given as following:

$$U = \begin{pmatrix} 1 & 0 & 0 \\ 0 & c_{23} & s_{23} \\ 0 & -s_{23} & c_{23} \end{pmatrix} \begin{pmatrix} c_{13} & 0 & s_{13}e^{-i\delta_{CP}} \\ 0 & 1 & 0 \\ -s_{13}e^{i\delta_{CP}} & 0 & c_{13} \end{pmatrix} \begin{pmatrix} c_{12} & s_{12} & 0 \\ -s_{12} & c_{12} & 0 \\ 0 & 0 & 1 \end{pmatrix}, \tag{1.2}$$

where $c_{ij} = \cos\theta_{ij}$, $s_{ij} = \sin\theta_{ij}$. The θ_{ij} is mixing angle and δ_{CP} is the CP violation phase. The probability of the neutrino oscillation from ν_α to ν_β after traveling distance L with the energy E is given as follows:

$$\begin{aligned} P(\nu_\alpha \to \nu_\beta) = \delta_{\alpha\beta} &- 4\sum_{i>j} Re(U^*_{\alpha i}U_{\beta i}U_{\alpha j}U^*_{\beta j})\sin^2\left(\frac{\Delta m^2_{ij}L}{4E}\right) \\ &- 2\sum_{i>j} Im(U^*_{\alpha i}U_{\beta i}U_{\alpha j}U^*_{\beta j})\sin\left(\frac{\Delta m^2_{ij}L}{2E}\right), \end{aligned} \tag{1.3}$$

where $\Delta m^2_{ij} = m^2_i - m^2_j$. The existence of neutrino oscillation indicates non zero Δm^2_{ij} and existence of flavor mixing. Especially, the equation for electron neutrino appearance from muon neutrino $P(\nu_\mu \to \nu_e)$ is given as follows:

$$
\begin{aligned}
P(\nu_\mu \to \nu_e) &= P1 + P2 + P3 + P4 \\
P1 &= \sin^2(\theta_{23}) \sin^2(2\theta_{13}) \sin^2(\Delta m^2_{32} L/4E) \\
P2 &= \cos^2(\theta_{23}) \sin^2(2\theta_{13}) \sin^2(\Delta m^2_{21} L/4E) \\
P3 &= \mp J \sin^2(\Delta m^2_{32} L/4E) \sin(\Delta m^2_{21} L/4E) \\
P4 &= J \cot(\delta_{CP}) \sin(\Delta m^2_{32} L/4E) \cos(\Delta m^2_{21} L/4E),
\end{aligned} \tag{1.4}
$$

where

$$
J = \cos(\theta_{13}) \sin(2\theta_{12}) \sin(2\theta_{13}) \sin(2\theta_{23}) \sin(\delta_{CP}) \tag{1.5}
$$

and the sign in P3 is negative for neutrino and positive for anti-neutrino. CP violation term can be measured comparing electron neutrino appearance probabilities with anti-neutrino as following:

$$
\begin{aligned}
P(\nu_\mu \to \nu_e) - P(\bar{\nu}_\mu \to \bar{\nu}_e) = &- 2 \sin(\delta_{CP}) \cos(\theta_{13}) \sin(2\theta_{12}) \sin(2\theta_{13}) \sin(2\theta_{23}) \times \\
&\sin^2(\Delta m^2_{32} L/4E) \sin(\Delta m^2_{21} L/4E).
\end{aligned} \tag{1.6}
$$

The measurement of CP violation phase is one of the most important measurement for long-baseline accelerator experiment.

1.2 Neutrino-Nucleus interaction

Comprehension of neutrino-nucleus interaction is essential for neutrino oscillation analysis as the reconstruction of initial neutrino energy and the selection of the signal event and the background event is based on neutrino-nucleus interaction. Neutrino-nucleus interaction mainly consists of two parts. First is the interaction of a neutrino with a nucleon through charged current (CC) mediated by $W^\pm$ boson or through neutral current (NC) mediated by Z boson to produce secondary particles. Second is the interaction of secondary particles with the nucleons in nucleus.

In order to detect neutrinos and determine their flavor, CC interactions must be used as signals. For the range of neutrino energy taken in WAGASCI experiment, up to 1 GeV, the CC interactions are dominant as shown in Figure 1.1. Charged current interaction is classified into several types[3].

- CC quasi-elastic

  Charged current quasi elastic (CCQE) scattering is the dominant neutrino interaction for neutrino energy less than about 1 GeV. CCQE process is shown as follows: $\nu_l + n \to l + p (\bar{\nu}_l + p \to l + n)$, where $l = e, \mu, \tau$. A single charged lepton and a nucleon are produced in the interaction of a neutrino (anti-neutrino) with a nucleon in the target materials. Because this process is two-body scattering,

the neutrino energy can be reconstrucred from the kinematics of both of the outgoing charged lepton and the nucleon. Also neutrino energy can be reconstructed from the outgoing charged lepton kinematics alone when the direction of initial neutrino is known.

- CC single π

  CC1π is the second dominant neutrino interaction for neutrino energy less than about 1 GeV. CC1π process is shown as follows: $\nu_l + N \rightarrow l + N' + \pi$. An inelastic scattering produces a nucleon excited state, mainly Δ resonance, and such a baryonic resonance quickly decays to a nucleon and single pion. Because this process is three-body scattering, the energy of scattered particles is likely to be lower than that produced in the CCQE process. If the pion or a nucleon fails to be reconstructed, this process can be main background.

- CC DIS

  CC deep inelastic scattering (DIS) is the dominant interaction for high energy neutrino. CC DIS process is shown as follows: $\nu_l + N \rightarrow l + N' + hadrons$. The process can be approximated to be the scattering of a neutrino with a quark. The cross section is small for neutrino energy less than about 1 GeV.

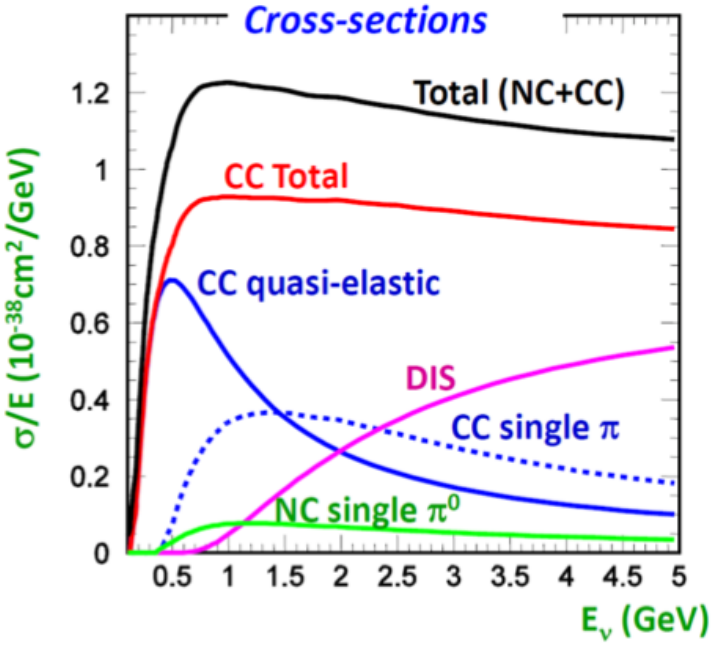

Fig. 1.1: The cross section of neutrino interaction in sub-GeV range[4].

The neutrino-nucleus interaction also depends on the kind of the target nucleus because the binding energy of the nucleon in nucleus affects the kinematics of secondary particles and initial nucleon. It is highly dependent on the nucleon kinematics model,

and the relativistic fermi gas (RFG) model is the principal model of current leading long-baseline experiment, T2K[5]. The RFG model is the assumption that all nucleons are in a potential and all states are filled up to a Fermi-level.

The interaction of secondary particles with nucleons in nucleus depends on the kind of nucleus and kinematics of the secondary particle . The outgoing charged lepton is almost not affected. Secondary hadrons such as pion and nucleon are strongly affected however. There is a possibility that hadrons are trapped in nucleus and then the kinematic is affected.

Current neutrino experiments use the nucleus which has multi nucleons such as carbon and oxygen as the target nucleus and neutrino-nucleus interaction plays an important role in the neutrino oscillation analysis. Hence, the cross-section measurement is important for precise neutrino oscillation measurements.

1.3 Current status of neutrino oscillation measurement

Current status of neutrino oscillation parameter is shown in Table 1.1[6]. The result is obtained by analyzing the solar neutrino data, long baseline accelerator experiment data, reactor neutrino data and atmospheric neutrino data.

Parameter	best-fit	3σ range
Δm^2_{21} $[10^{-5}\mathrm{eV}^2]$	7.50	7.03-8.09
$\Delta m^2_{31(32)}$ $[10^{-3}\mathrm{eV}^2]$	2.524(2.514)	2.407-2.643(2.399-2.635)
$\sin^2\theta_{12}$	0.306	0.271-0.345
$\sin^2\theta_{23}$	0.441(0.587)	0.385-0.635(0.393-0.640)
$\sin^2\theta_{13}$	0.02166(0.02179)	0.01934-0.02392(0.01953-0.02408)
δ/π	1.45(1.53)	1.12-1.73(1.28-1.76)

Table 1.1: The best-fit values and 3σ allowed ranges of the 3-neutrino oscillation parameters, derived from a global fit of the current neutrino oscillation data(from[7]). For the CP violation phase δ the best fit value and the 1σ allowed range is given. The values (values in brackets) correspond to $m_1 < m_2 < m_3$ ($m_3 < m_1 < m_2$)

1.4 T2K experiment

The Tokai to Kamioka (T2K) experiment, shown in Figure 1.2, is a long-baseline neutrino oscillation experiment with the neutrino beamline produced in Japan Accelerator Research Comprex (J-PARC). It has started in 2009[8]. The neutrino beam is measured by a near detector (ND280) located at 280 m downstream from the beam target and a far detector, Super-Kamiokande (SK), at 295 km downstream. T2K adopts

the off-axis method, which allows the neutrino beam to have a narrow band flux with its peak shifted to lower energy. The 2.5° off-axis angle used in T2K gives a narrow peak around at 600 MeV as shown in Figure 1.3.

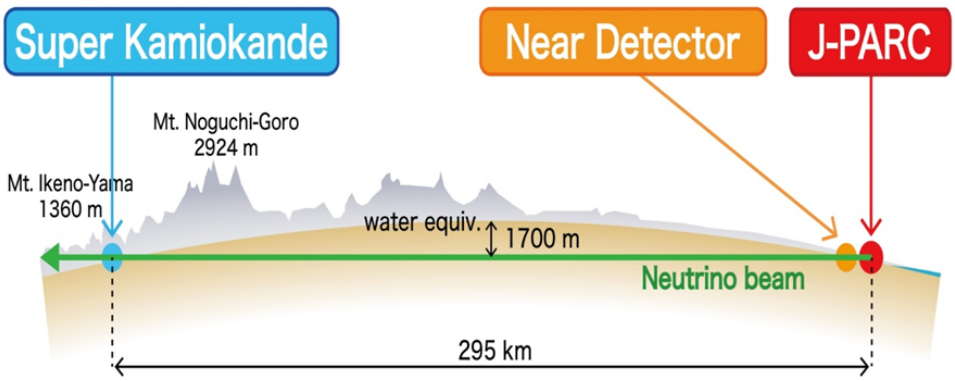

Fig. 1.2: A overview of T2K experiment.

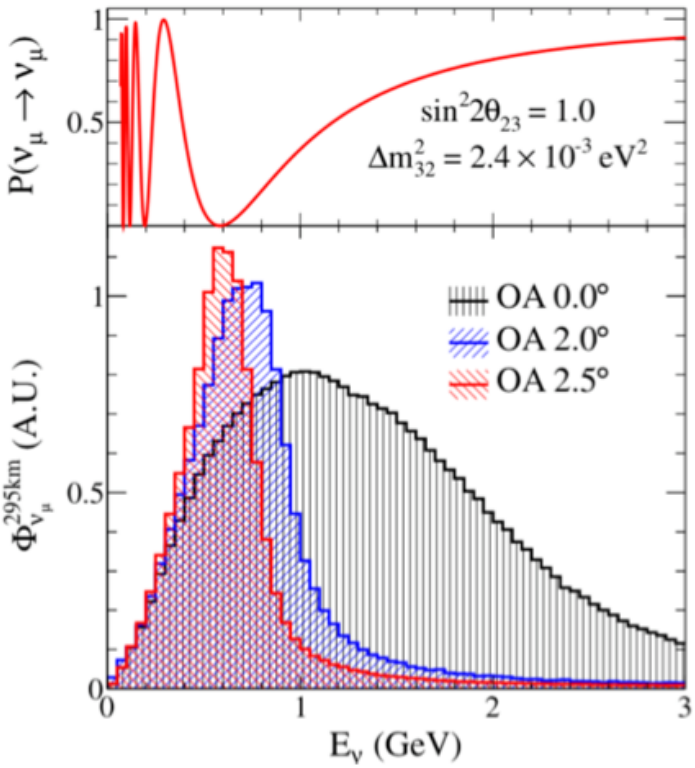

Fig. 1.3: The oscillation probability (top) and neutrino energy spectrum (bottom)[13].

1.4.1 J-PARC Neutrino beam

J-PARC consists of three accelerators[9], a linear accelerator (LINAC), a rapid-cycling synchrotron (RCS) and a main ring (MR) synchrotron. The proton beam injected into MR is accelerated up to 30 GeV. Each proton beam spill extracted to the T2K neutrino beamline from MR consists of eight bunches. The proton beam impinges into a graphite target to produce secondary pions, which are focused by three magnetic horns and decay in flight into muons and muon neutrinos:

$$\pi^+ \to \mu^+ + \nu_\mu \tag{1.7}$$

$$\pi^- \to \mu^- + \bar{\nu}_\mu. \tag{1.8}$$

The neutrino beam is dominated by ν_μ when the magnetic horns are excited with 250 kA current (neutrino mode), while it is dominated by $\bar{\nu}_\mu$ with the -250 kA horn current (anti-neutrino mode). All hadrons, as well as muons below about 5 GeV/c, are stopped by the beam dump, and neutrinos penetrate through the beam dump to be measured by the detectors.

High energy muons penetrating the beam dump are monitored by MUMON[10], a detector placed behind the beam dump, to indirectly monitor the neutrino beam direction on a spill-by-spill bases.

1.4.2 Near detectors

T2K adopts two near detectors, on-axis and off-axis detectors. Both on-axis and off-axis detectors are placed at 280 m downstream from the neutrino beam target.

The on-axis near detector, INGRID[11], measures the direction, profile and event rate of neutrino beam. The center position of INGRID is set at the center of neutrino beam. The on-axis detector provides constraints on the beam direction with the precision better than 10 cm, which corresponds to 0.4 mrad precision at 280 m downstream from neutrino beam target. INGRID consists of 14 identical modules arranged as a cross of two identical groups along the horizontal and vertical direction. A module is composed of a sandwich structure of 11 tracking planes and 9 iron plates.

The off-axis detector, ND280, measures the event rate of neutrino beam. ND280 is placed on the same angle as SK and provides constraints on the neutrino beam flux and cross section. ND280 consists of the magnet and several detectors inside the magnet. The two fine-grain detectors (FGDs), which consist of tracking planes of scintillator bars, are the active targets and are sandwiched by three time production chambers (TPCs). ND280 measures the charged current interaction in FGDs and the acceptance is restricted to forward scattering due to its geometrical structure.

1.4.3 Far detector

The far detector, Super-Kamiokande[12], measures the energy and event rate of ν_e ($\bar{\nu}_e$) appearance and the ν_μ ($\bar{\nu}_\mu$) disappearance by detecting Cherenkov light emitted

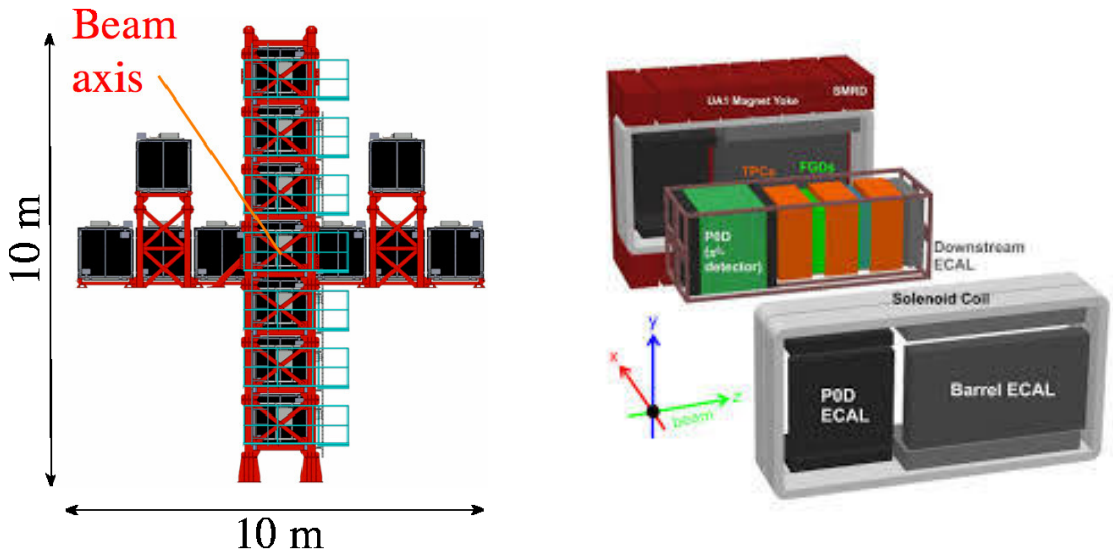

Fig. 1.4: The view of near detectors, on-axis detector (INGRID) (left) and off-axis detector (ND280) (right).

by a charged lepton produced in neutrino interaction in water. SK consists of stainless tank, sized 39 m diameter and 42 m tall, and 5,000 tons pure water and a large number of photomultiplier tubes (PMTs) which cover inside inner tank as shown in Figure 1.5. The acceptance is 4π.

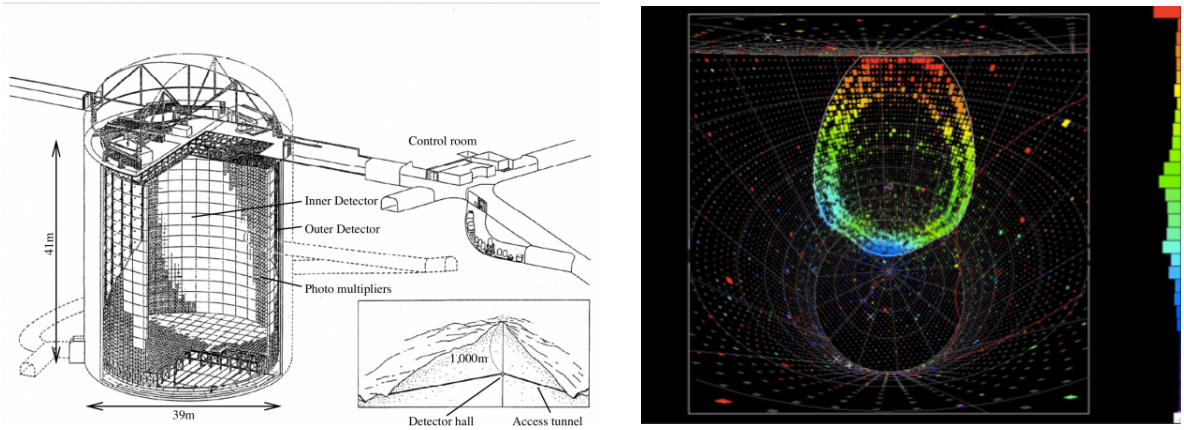

Fig. 1.5: The view of far detectors, Super-Kamiokande (left) and Cherenkov ring image of electron event (right).

2 WAGASCI experiment

WAGASCI experiment is proposed to measure the charged current neutrino cross section ratio between water and hydrocarbon with large angular acceptance in order to reduce the uncertainties in the T2K neutrino oscillation analysis. The goals of this experiment are:

1. to measure the charged current cross section ratio of water to hydrocarbon with 3% uncertainty.
2. to measure the charged current cross section on water and hydrocarbon individually with large phase space.

2.1 Design of WAGASCI experiment

2.1.1 Full setup

The WAGASCI experiment has been conducted in the T2K neutrino near detector hall at J-PARC. The detectors are located on the 1.5° off-axis from the neutrino beam center, where the neutrino energy spectrum is a similar to that of T2K, on the 2.5° off-axis. Figure 2.1 shows the neutrino beam flux in terms of neutrino energy spectrum on 0.00°, 1.06°, 1.50° and 2.50°.

The detectors of WAGASCI experiment are composed of several modules as shown in Figure 2.2. The central module is an active target detector. It is composed of two modules which contain water and hydrocarbon targets. The side two modules are muon range detectors (SideMRDs) and main topic of this thesis. The downstream module is also muon range detector (BabyMIND) and magnetized in order to identify the charge of detected particle. Both of SideMRDs and BabyMIND consist of tracking planes and iron plates.

The detection method of each module is same although the size, mass and electronics are different. Each detector contains plastic scintillator bars. Charged particles passing scintillators generate scintillation light. The light is collected by the wave length shifting fibers (WLSFs) and then detected by multi-pixel photo counters (MPPCs), which are semiconductor detectors produced by Hamamatsu Photonics.

2.2 Detector design

2.2.1 Central detector

The central detector is composed of four modules, each of which contains 0.5 ton target, water or hydrocarbon, and plastic (hydrocarbon) scintillator bars. Figure 2.3 shows the side view of one of four modules. The volume of each module is $1 \times 1 \times 0.5$ m^3. The 3 mm thick scintillator bars form the three dimensional grid structure as

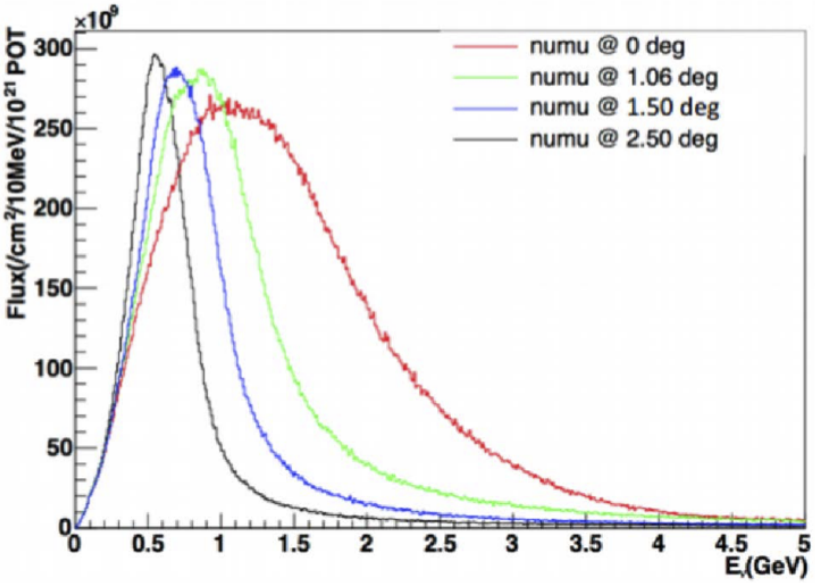

Fig. 2.1: The neutrino beam flux in terms of neutrino energy spectrums on 0.00°, 1.06°, 1.50°, 2.50°. The mean energy on 1.50° and 2.50° is about 600MeV.

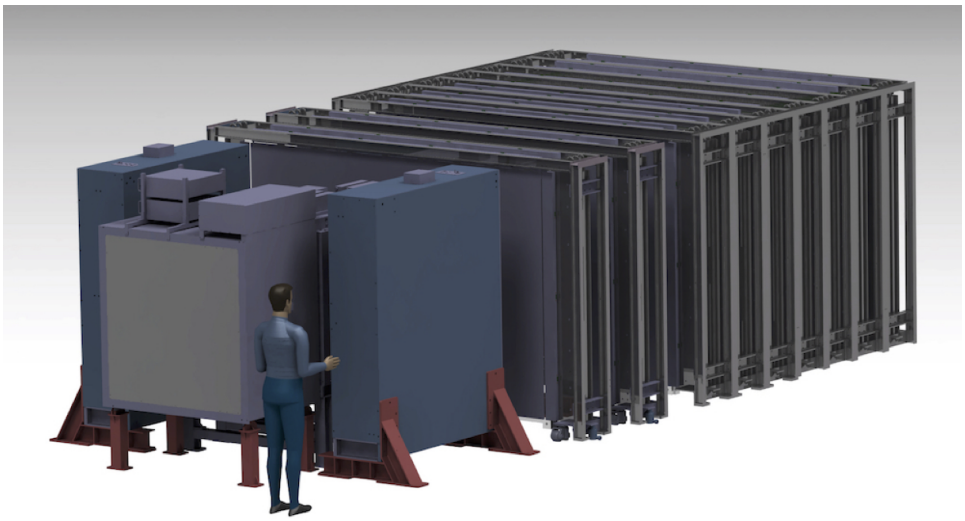

Fig. 2.2: A schematic view of WAGASCI detectors. It consists of central target detectors, side muon range detectors and downstream magnetized muon range detector.

shown in Figure 2.4, consisting of three different types of layers, X-layer, Y-layer and grid-layer. Water target fills the outer vessel and the scintillator bars are sunk inside it, while hydrocarbon target fills each cell of the grid structure with cubes. This structure allows the detector to realize a large fraction of the target volume as 80%, and to have a large acceptance with almost 4π solid angle for charged particles. The total target mass is one ton for each of water and hydrocarbon. The total number of scintillator channels in the central detector is 5,120.

A neutrino in the beam interacts with a nucleus of water target or hydrocarbon by charged current interaction, and a muon is generated with other particles. The scintillation light generated by energy deposits of the charged particles on each scintillator bar is collected through WLS fibers, and detected by MPPC. A track of the muon is reconstructed by the hit information in scintillators, and a vertex of the neutrino interaction is determined. Other charged particles from the neutrino interaction are also reconstructed, and used as additional information to determine the vertex. It is impossible to discriminate interaction on the scintillator bars from that on targets. This causes background events for cross section measurements, but the event rate is estimated by event rate of neutrino interactions on the hydrocarbon target.

The uncertainty of neutrino flux leads to large uncertainty in measurement of absolute cross section. It can be canceled by taking the ratio of cross section with the same neutrino flux. In order to reduce the difference in neutrino flux between the water and hydrocarbon targets, these two targets are placed every 50 cm alternatively along the z axis.

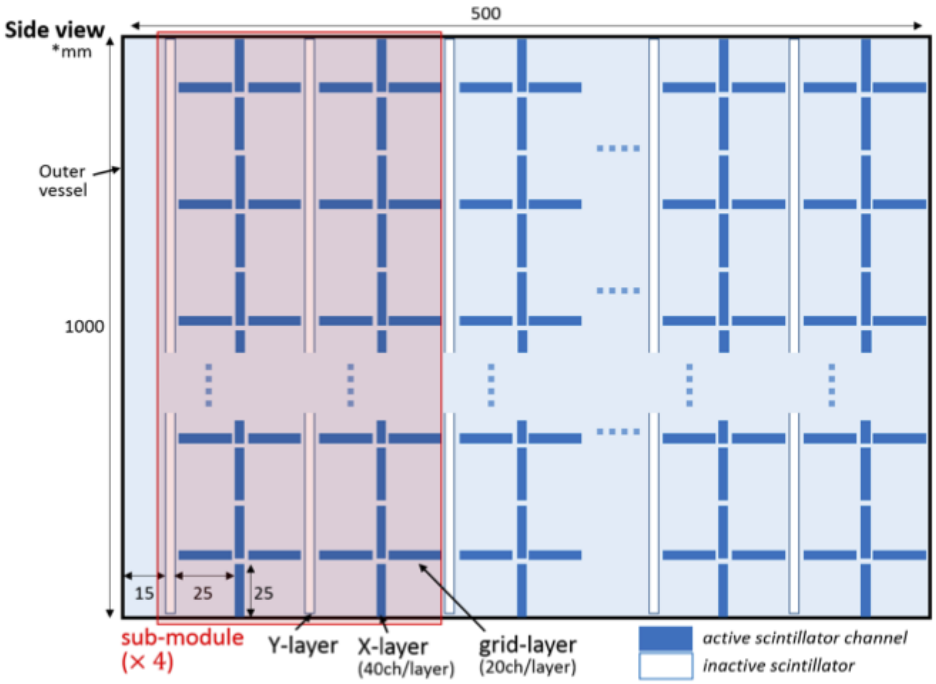

Fig. 2.3: One of four modules in the central detector.

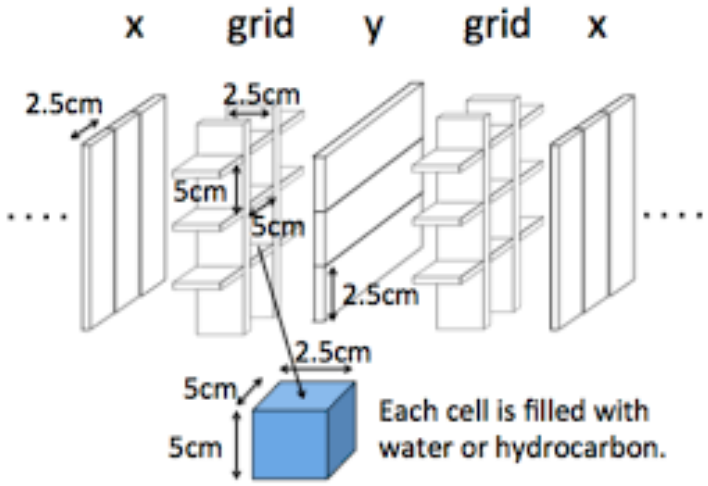

Fig. 2.4: The three-dimensional grid-like structure of the plastic scintillator inside of the central detector.

2.2.2 SideMRDs

The side muon range detectors, SideMRDs, consist of two modules which are placed at both sides of the central detector. Each module consists of sandwich structure of 11 iron plates and 10 tracking planes as shown in Figure 2.5. A iron plate is sized $30 \times 1610 \times 1800\,\mathrm{mm}^3$. A tracking plate is composed of 8 scintillator bars with the dimension of $7 \times 200 \times 1800\,\mathrm{mm}^3$. A scintillator bar is composed of mainly polystyrene and surrounded by reflector, and a sinusoidal groove is milled along a scintillator bar in order to provide uniform light collection over the whole scintillator surface. A wave length shifting fiber, which is same as one used for Water Module and 5 m in length, is glued with the optical cement in the S-shape groove. Both sides of fiber are glued into optical connector. The surface is polish and both sides are attached to MPPCs, S13081-050CS. A scintillator bar is covered with tyvec sheet and rubber with 3 mm thick in order to fix the bar in 13 mm gap between each iron plates. The MPPC signal is transported to a single MPPC card by a coaxial cable.

2.2.3 BabyMIND

The downstream muon range detector, BabyMIND[14], is the magnetized muon range detector which is placed for charge identification. BabyMIND consists of 33 iron modules and 18 tracking planes as shown in Figure 2.6. An iron modules is composed of an iron plate and coils. An iron modules is sized $3500 \times 2000 \times 50\,\mathrm{mm}^3$ and its weight is 1900 kg. The magnetic field is 1.5 T for current of 150 A and it is confirmed to be uniform over the central tracking region by the simulation as shown in Figure

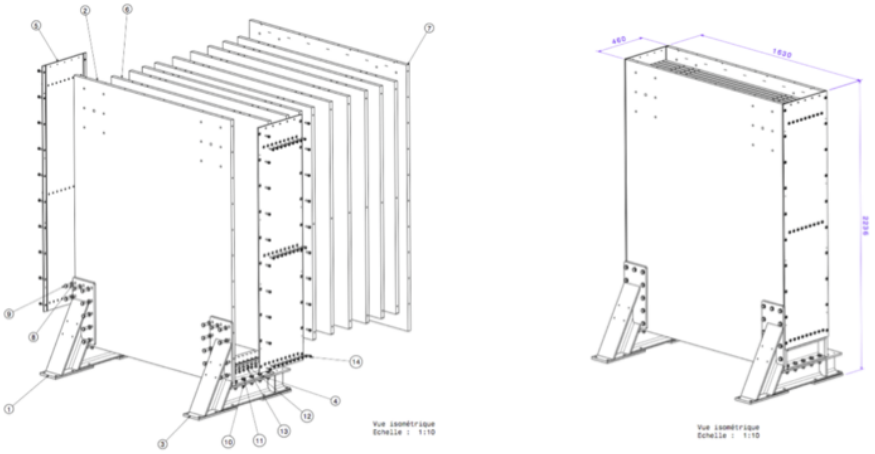

Fig. 2.5: A schematic view of SideMRD.

??. It is also confirmed by the test measurement with 9 pick-up coils.

A tracking plane is composed of 95 horizontal scintillator bars and 16 vertical scintillator bars. A horizontal bar is sized $2880 \times 31 \times 7.5\text{mm}^3$ and has a groove along the long side of the bar to insert a wave length shifting fiber. A vertical bar sized $1950 \times 210 \times 7.5\text{mm}^3$ and U-shaped groove along the bar. The surface is polished and either side of a fiber of a horizontal bar is attached MPPCs, S12571-025C and both sides of a vertical bat are attached.

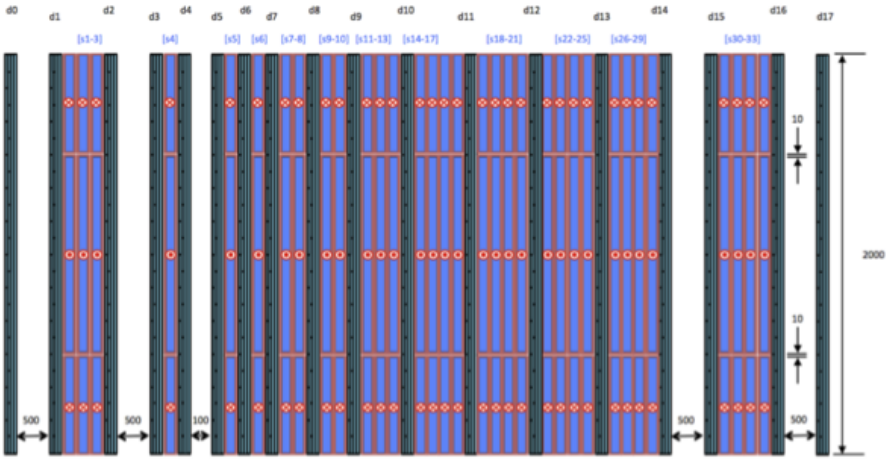

Fig. 2.6: The schematic view of BabyMIND with muons incident from the left. Scintillator modules are referenced d0 to d17, magnet modules are referenced s1 to s33.

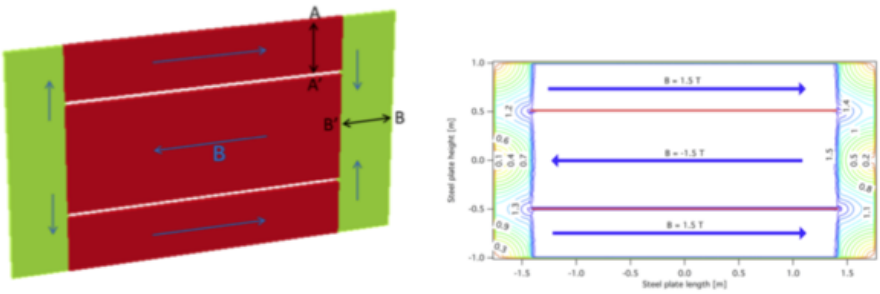

Fig. 2.7: Complete return of the magnetic flux requires cross-sections A-A ’ and B-B ’ to be equal (left). Magnetic field map with a 280cm long coil, 1.5kA (right figure).

3 Characteristics of MPPCs and scintillators

3.1 Characteristics of MPPCs

MPPC is one of the Silicon Photomultiplier (SiPM) developed by Hamamatsu-Photonics. It has multi pixels of Avalanche Photo Diode (APD) and quenching resistance. The output signal of one pixel is constant corresponding to one photon and called photon-equivalent (p.e.). The output of MPPC is proportional to number of pixels detecting photons as shown in Figure 3.1.

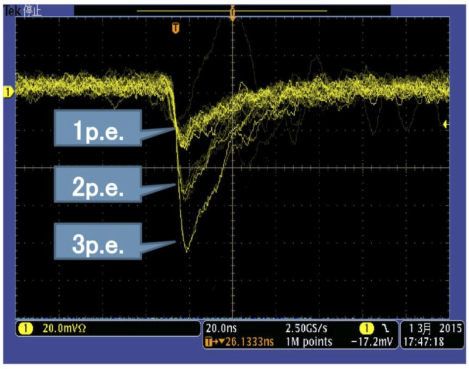

Fig. 3.1: The output signal of MPPC by oscilloscope.

The characteristic parameters of MPPC are as follows.

- Breakdown voltage and Over voltage
  MPPC operates as APD when the bias voltage is over the breakdown voltage. The over voltage ΔV is given as

$$\Delta V = V_{bias} - V_{br}, \tag{3.1}$$

  where V_{bias} is the bias voltage and V_{br} is the breakdown voltage. The typical operation voltage of MPPC is set with $\Delta V = 3.0$V.

- Gain
  Gain of MPPC is approximately proportional to the over voltage. The output charge of a pixel is given as

$$Q_{1p.e.} = C\Delta V, \tag{3.2}$$

where C is a capacitance of MPPC. Figure 3.2 shows the charge distribution of MPPC measured by ADC. Each peaks are corresponding to pedestal, 1p.e., 2 p.e. and so on. Gain is calculated by the distance of two neighboring peaks as

$$Gain[\text{ADC count}] = M_{i+1} - M_i, \tag{3.3}$$

where M_i is the mean ADC count of i-th peak. The position of a peak is obtained by fitting the peak by gaussian.

- Dark noise

  Though no light is injected to MPPC, electron-hole pair is sometimes thermally excited and induces avalanche multiplication in a pixel of MPPC, and MPPC outputs charge corresponding to 1 p.e.. Basically, dark noise is detected as 1 p.e. and can't be distinguished with the signal of a photoelectron occurred from a photon. Dark noise is measured as the output of MPPC without light injection, and dark noise rate is calculated as

$$Dark\ noise\ rate[\text{Hz}] = \frac{N_{0.5p.e.}}{T}, \tag{3.4}$$

  where $N_{0.5p.e.}$ is the number of entries that the charge is over 0.5 p.e. and T is the measurement time.

- Crosstalk

  In case that a excited electron generated in a pixel moves to a neighboring pixel, the output of 1 p.e. is mistaken as 2 p.e.. It is called crosstalk. Crosstalk rate is calculated with the same conditions as the measurement of dark noise rate as

$$Crosstalk\ rate[\%] = \frac{N_{1.5p.e.}}{N_{0.5p.e.}}, \tag{3.5}$$

  where $N_{1.5p.e.}$ is the number of entries that the charge is over 1.5 p.e..

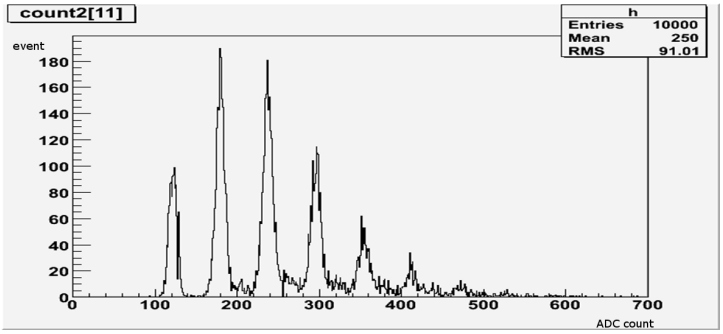

Fig. 3.2: ADC distribution of MPPC with LED injection.

The specificatitions of single MPPCs used in SideMRDs, named S13360-1350C, is listed on Table 3.1. Figure 3.3 shows the single MPPC and an enlarged view of a channel.

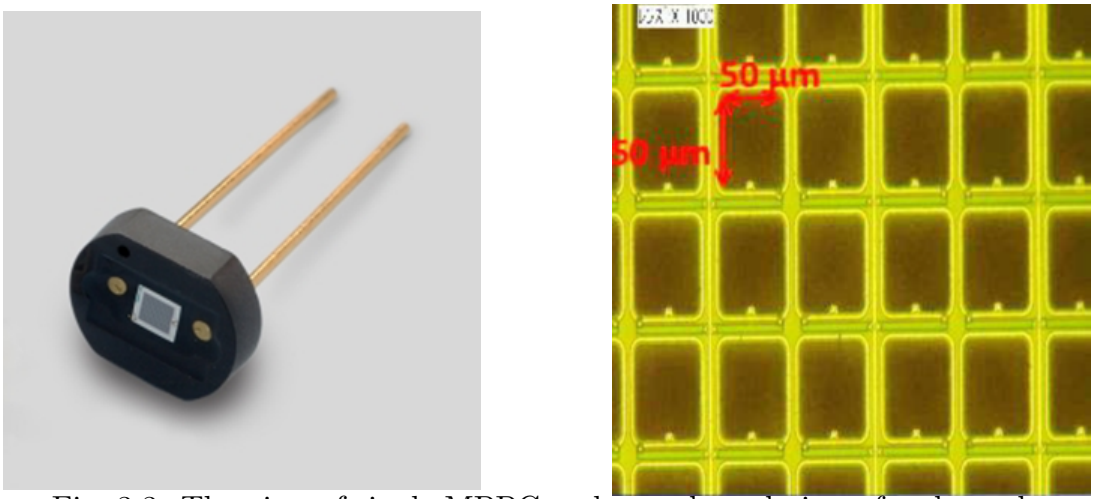

Fig. 3.3: The view of single MPPC and an enlarged view of a channel.

number of pixels	667
pixel picth	50 μm
size of sensitive area	1.3 mm $\times$ 1.3 mm
operation tempurature	-20 - 60 °C
sensitive fluequency range	270 - 900 nm
operation voltage (type.)	53 $\pm$ 5 V
dark noise rate (type.)	90 kHz
crosstalk probability (type.)	1%

Table 3.1: Basic characteristic of MPPC reported by Hamamatsu Photonics.

3.2 Performance of scintillators

The scintillators used in SideMRD were produced at INR and transported to Yokohama National University (YNU), and their performance was measured[15]. The characteristics of scintillator are that the scintillation light is measured at both side and the WLS fiber whose length is 5.4 m and diameter is 1 mm is glued in S-shape to get an uniform response over the scintillator. At the end of scintillator, WLS fiber is cut and polished, and attached with optical connector male. It is connected with MPPC attached with optical connector female. The length of scintillator along the glued fiber is 1800 mm as shown in Figure 3.4. In order to reconstruct the track of muon entering into SideMRD, position resolution along a scintillator is essential. Time resolution is also important to distinguish the motion direction of the track.

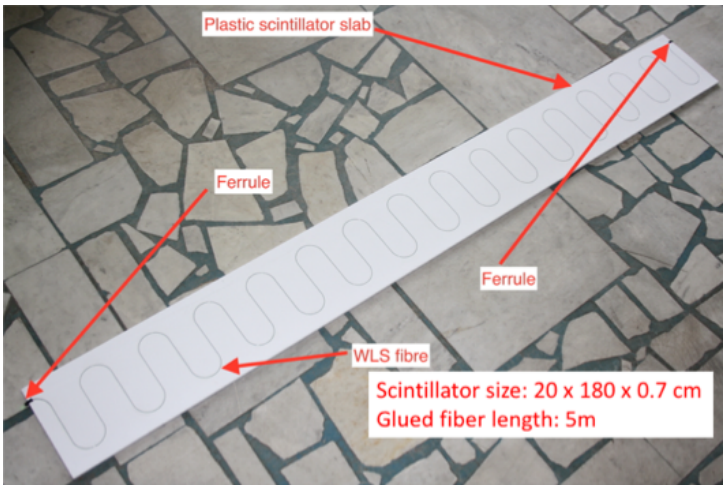

Fig. 3.4: A view of scintillator used in SideMRD.

3.2.1 Test measurement with cosmic ray

The charge and time of a scintillator are measured by CAMAC modules, ADC and TDC. For preparatory measurement, the performances of ADC and TDC were measured for two MPPCs. To get gains of two MPPCs as ADC count, LED light was used and the gains ware calculated by Equation 3.3. The relation between time and TDC count were also obtained by measuring TDC count changing the time injected to TDC.

The setup for main measurement is shown in Figure 3.5. For trigger, NaI (TI) scintillator and Photomultiplier are used. NaI scintillator size is $60\times60\times170$ mm^3. Two triggers are set on top and bottom of scintillator perpendicularly. The position of triggers is variable. In case that two triggers get signal at the same time, gate signal is generated and the charge and time information of the signals coming from two MPPCs are converted to digital value by ADC and TDC.

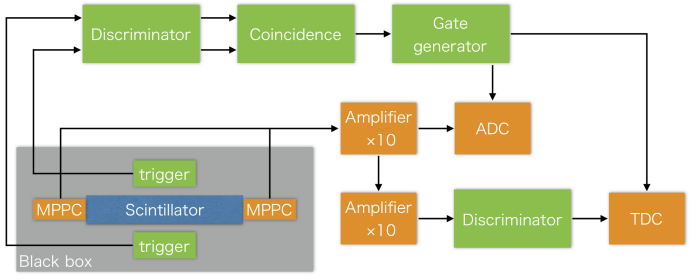

Fig. 3.5: Setup for performance test of scintillator.

The light yield is calculated from ADC count as

$$L.Y.[\text{p.e.}] = \frac{charge[\text{ADC count}] - pedestal[\text{ADC count}]}{gain[\text{ADC count}]}. \tag{3.6}$$

Figure 3.6 shows the time distribution of both side when the trigger position is at the center of scintillator. Tail appears in earlier range due to delay of scintillation light emission of NaI scintillators. Figure 3.7 shows T_{dif} and T_{mean} distribution with the trigger position at the center, where $T_{dif} = \frac{T_L - T_R}{2}$, $T_{mean} = \frac{T_L + T_R}{2}$, T_L is the time measured at the light side of scintillator and T_R is at the right side.

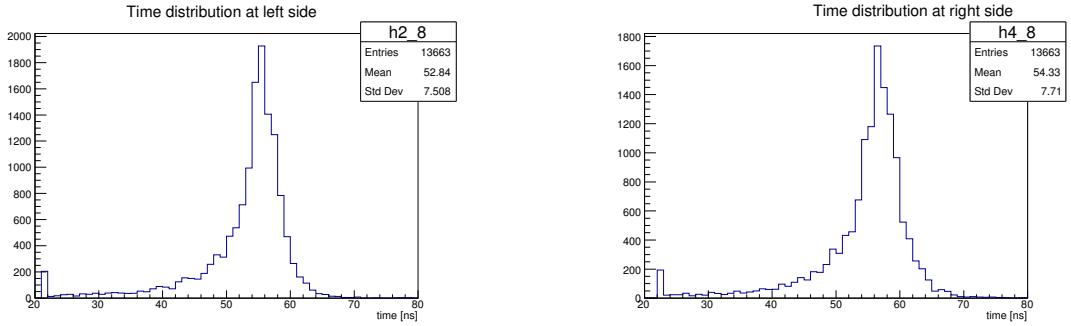

Fig. 3.6: Time distribution at left side (left) and right side (right) with the trigger position at center of scintillator.

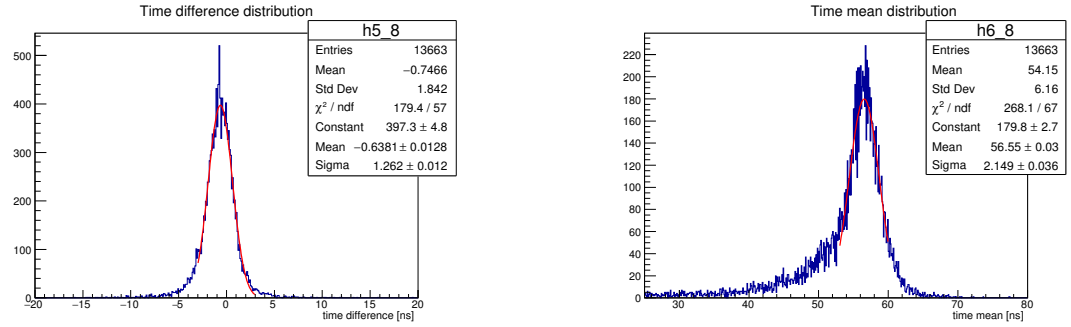

Fig. 3.7: Time difference distribution (left) and time mean distribution (right) with the trigger position at center of scintillator.

By taking the mean of these distribution changing the position of trigger along the scintillator from -80 cm to 80 cm by 10 cm, the correlations are obtained. The hit position of cosmic particle approximates to the center position of trigger by taking the mean. Figure 3.8 shows that T_{dif} is proportional to the hit position. The correlation function is obtained by fitting the correlation by linear function as follows:

$$T_{dif}[\text{ns}] = (0.1928 \pm 0.0029) \times X[\text{cm}] - 0.77 \pm 0.14, \tag{3.7}$$

where X is the hit position. The velocity of a signal along the scintillator is obtained by Equation 3.7 as

$$v_{sci} = 5.2 \text{ cm/ns}. \tag{3.8}$$

Figure 3.9 is the correlation between RMS of T_{dif} and the position of trigger. RMS of T_{dif} is obtained by fitting T_{dif} distribution by gaussian. The RMS is constant independent from the position. The mean value of the RMS is obtained as

$$\sigma_{T_{dif}} = 1.29 \text{ ns}. \tag{3.9}$$

$\sigma_{T_{dif}}$ includes dispersion due to the wide range of trigger.

Measured timing T is divided into four parameters as following:

$$T = T_{sci} \pm T_{tri} + T_{elec} - T_0, \tag{3.10}$$

where T_{sci} is the time that the scintillation light traveling from center position of trigger to MPPC, T_{tri} is the time that the light traveling from hit position to center of trigger and the sign of T_{tri} is whether hit position is at left side of center of trigger or at right side, T_{elec} is the time signal traveling from MPPC to TDC and T_0 is time zero defined by trigger signal and TDC. Then T_{dif} is described as follows:

$$\begin{aligned} T_{dif} &= \frac{T_L - T_R}{2} \\ &= \frac{T_{sci\_L} - T_{sci\_R}}{2} \pm \frac{T_{tri\_L} - T_{tri\_R}}{2} + \frac{T_{elec\_L} - T_{elec\_R}}{2} - \frac{T_{0\_L} - T_{0\_R}}{2} \\ &\quad \frac{T_{sci\_L} - T_{sci\_R}}{2}, \end{aligned} \tag{3.11}$$

Because $T_{elec\_L} - T_{elec\_R}$ and $T_{0\_L} - T_{0\_R}$ are zero consistent independent from events, the RMS of T_{dif} is also calculated as follows:

$$\begin{aligned} \sigma_{T_{dif}} &= \sqrt{\frac{\sigma^2_{T_{sci\_L}-T_{sci\_R}} + \sigma^2_{T_{tri\_L}-T_{tri\_R}} + \sigma^2_{T_{elec\_L}-T_{elec\_R}} + \sigma^2_{T_{0\_L}-T_{0\_R}}}{4}} \\ &= \sqrt{\frac{\sigma^2_{T_{sci}} + \sigma^2_{T_{tri}}}{2}}. \end{aligned} \tag{3.12}$$

Assuming that hit position in the trigger is random, the RMS of position in trigger is calculated as $\frac{d}{\sqrt{12}}$, where d is the range of random hit, 6 cm. From Equation 3.7, $\sigma_{T_{tri}}$ is obtained as 0.33 ns. According to the above calculation, $\sigma_{T_{sci}}$ is obtained as

$$\sigma_{T_{sci}} = 1.79ns. \tag{3.13}$$

It is the time resolution of a scintillator.

Figure 3.10 shows that T_{mean} is constant independent from the hit position. The mean value of T_{mean} is obtained as follows:

$$T_{mean} = (53.915 \pm 0.078) \text{ ns}, \tag{3.14}$$

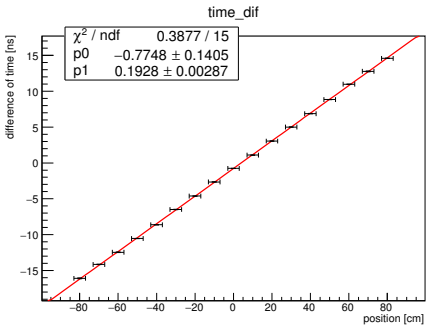

Fig. 3.8: Correlation between difference of time and hit position. X axis is center position of trigger and Y axis is difference of times at two sides.

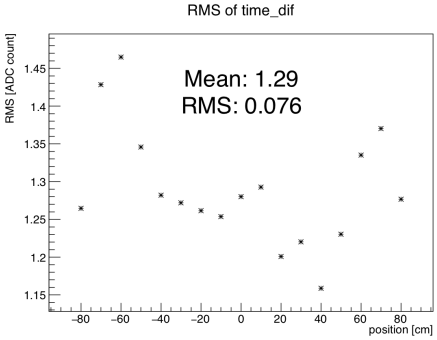

Fig. 3.9: RMS of time difference for each hit position. X axis is center position of trigger and Y axis is RMS of time difference obtained by gaussian fitting.

Figure 3.11 is the correlation between RMS of T_{mean} and the position of trigger. RMS of T_{mean} is obtained by fitting T_{mean} distribution by gaussian. The RMS is constant independent from the position. The mean value of the RMS is obtained as

$$\sigma_{T_{mean}} = 2.04 \text{ ns}. \tag{3.15}$$

$\sigma_{T_{mean}}$ is more than $\sigma_{T_{dif}}$ because the trigger timing dispersion is large due to bad time resolution of NaI scintillator.

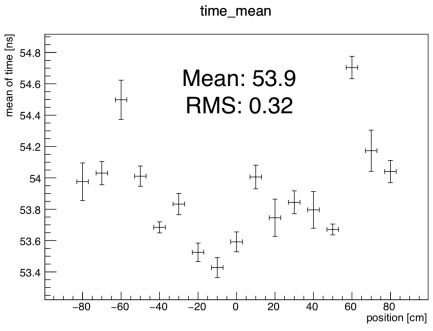

Fig. 3.10: Correlation between mean of time and hit position. X axis is center position of trigger and Y axis is mean of times of two sides.

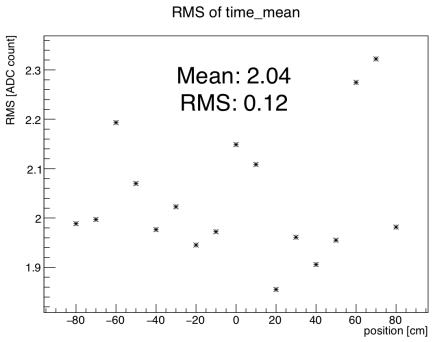

Fig. 3.11: RMS of time mean for each hit position. X axis is center position of trigger and Y axis is RMS of time mean obtained by gaussian fitting.

Figure 3.12 shows the light yield distribution of both sides when the trigger position is at the center of scintillator. The correlation between mean of the light yield of both sides and trigger position is shown in Figure 3.13. They are fitted by exponential function corresponding to decay of the light yield traveling in scintillator and WLS

fiber. Figure 3.14 shows LY_{sum} and LY_{assy} distribution with the trigger position center, where $LY_{sum} = LY1 + LY2$, $LY_{assy} = \frac{LY2-LY1}{LY1+LY2}$, $LY1$ is the light yield measured at the left side of scintillator and $LY2$ is at the right side.

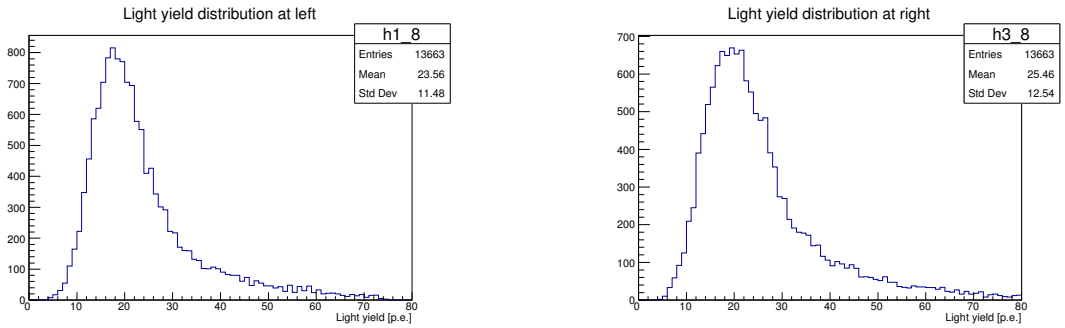

Fig. 3.12: Light yield distribution at left side (left) and right side (right) with the trigger position at center of scintillator.

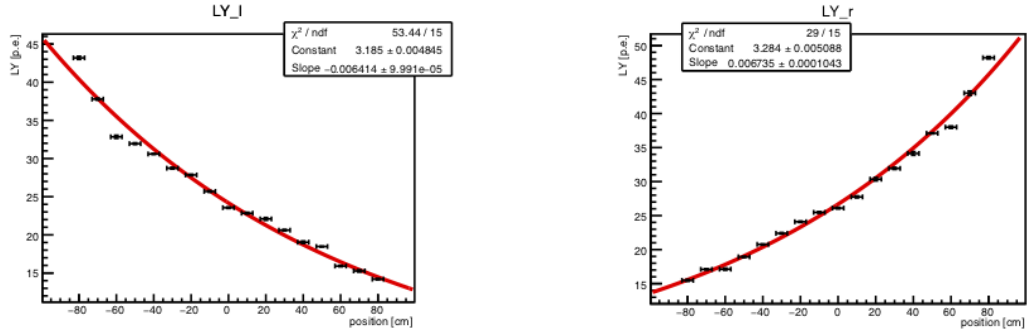

Fig. 3.13: Correlation between light yield and hit position at left side (left) and right side (right). X axis is center position of trigger and Y axis is light yield.

By taking the mean of these distribution changing the position of trigger along the scintillator from -80 cm to 80 cm by 10 cm, the correlations are obtained. Figure 3.15 is the correlation between mean of LY_{sum} and the position of trigger. The correlation function is obtained as

$$LY_{sum} = (1.726 \pm 0.076) \times 10^{-3} \times X^2 - (0.0046 \pm 0.0029) \times X + 46.696 \pm 0.094 \quad (3.16)$$

The mean of LY_{sum} of the scintillator is about 50 p.e..

Figure 3.16 shows that mean of LY_{assy} is approximately proportional to the hit position. The correlation function is obtained by fitting it by linear function as

$$LY_{assy} = (6.136 \pm 0.091) \times 10^{-3} \times X - 0.0613 \pm 0.0045. \quad (3.17)$$

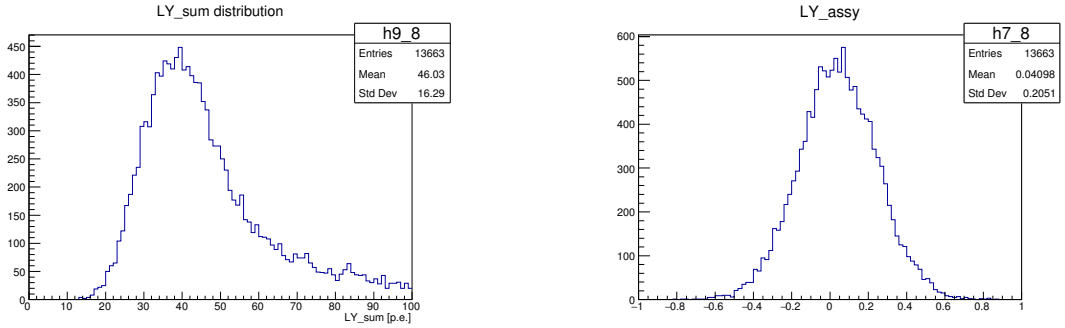

Fig. 3.14: Light yield sum distribution (left) and light yield asymmetry distribution (right) with the trigger position at center of scintillator.

Figure 3.17 is the correlation between RMS of LY_{assy} and the position of trigger. Position resolution of scintillator along X-axis is calculated by Equation 3.17 as shown in Figure 3.18. If hit position is determined by asymmetry of light yield, the resolution is about 40 cm.

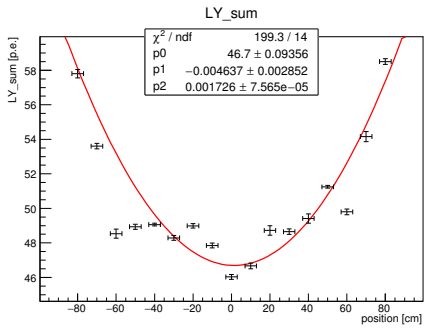

Fig. 3.15: Correlation between LY_sum and hit position. X axis is center position of trigger and Y axis is sum of light yield of both sides.

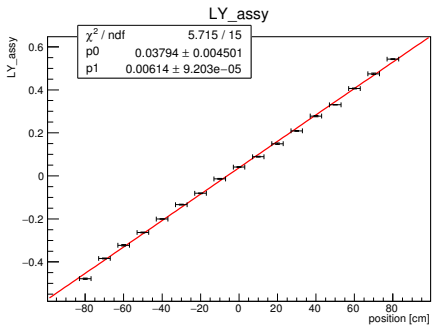

Fig. 3.16: Correlation between LY_assy and hit position. X axis is center position of trigger and Y axis is asymmetry of light yield of both sides.

3.2.2 Mass measurement with cosmic ray

The performance of scintillators are measured for 324 scintillators. The setup for mass measurement is shown in Figure 3.19. Trigger system is same as test measurement but four scintillators are measured at the same time. Instead of CAMAC modules, ADC and TDC, 16+1 channel CAEN digitizer DT5742 (called digitizer in this thesis) is used. Digitizer measures the signal during 200 ns, and the data is hold on 1024 capacitor cells. 1 TDC count is 200/1024 ns. The charge of each cells is converted to digital value by 12-bit ADC. Figure 3.20 shows a typical waveform of a cosmic event obtained

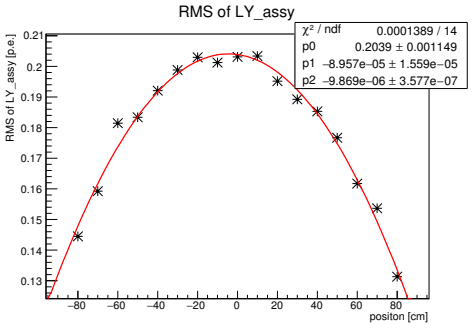

Fig. 3.17: Correlation between RMS of LY_sum and hit position. X axis is center position of trigger and Y axis is RMS of sum of light yield.

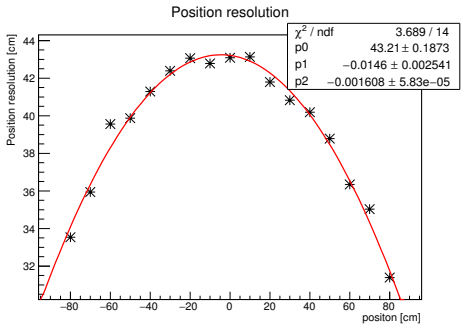

Fig. 3.18: Correlation between position resolution and hit position. X axis is center position of trigger and Y axis is position resolution obtained by the equation between RMS of LY_assy and position.

by digitizer.

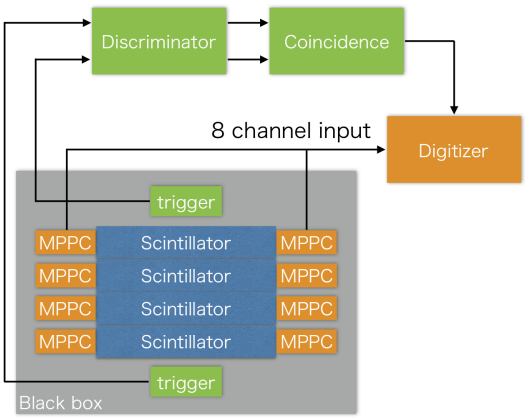

Fig. 3.19: Setup for performance test of scintillator.

The light yield distributions for both sides are measured by changing the position of triggers for 4 scintillators at the same time. The correlation between the mean light yield of 4 scintillators and trigger position for each side is shown in Figure 3.21. Figure 3.22 shows the correlation between mean LY_{sum} of the 4 scintillators and the position of trigger. Figure 3.23 shows the correlation between mean LY_{assy} of the 4 scintillators and the position of trigger. The correlation function is obtained by fitting it by linear function as

$$LY_{assy} = (4.510 \pm 0.073) \times 10^{-3} \times X + 0.0708 \pm 0.0034. \tag{3.18}$$

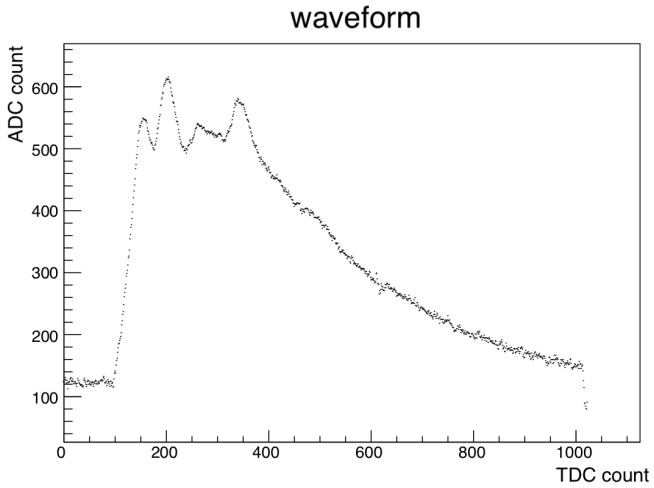

Fig. 3.20: A typical waveform of a cosmic signal by digitizer. X axis is TDC count and Y axis is ADC count. 1024 TDC counts correspond to 200 ns.

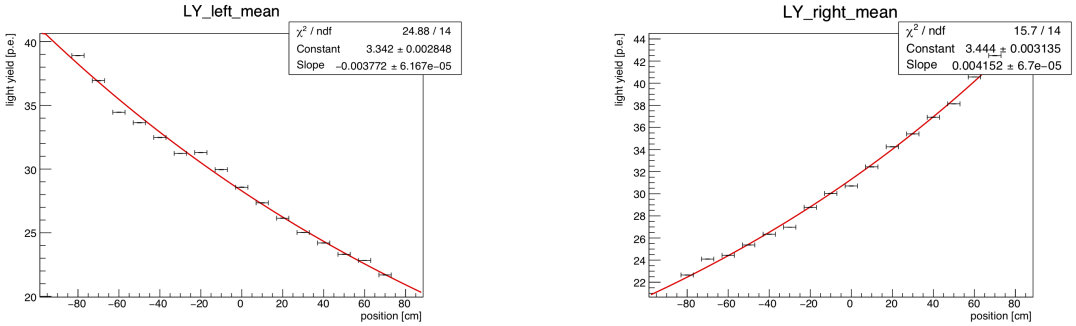

Fig. 3.21: Correlation between light yield and hit position for the left side (left) and right side (right). X axis is center position of trigger and Y axis is light yield.

LY_{sum} and LY_{assy} are measured for 324 scintillators with trigger position fixed at center of the scintillator. Figure 3.24 and 3.25 show the distribution of LY_{sum} and LY_{assy}. The mean of LY_{sum} is calculated to be about 40 p.e. and the RMS of the light yield is 10%. Scintillation light yield generated by a minimum ionized particle passing through a scintillator is estimated to be about 20 p.e..

3.2.3 summary

The performance of scintillators are measured. The scintillator is glued with a WLS fiber in an S-curve shape, attached readout electronics at both sides and the size is $7\times200\times1800$ mm^3. The light yield of cosmic ray is about 20 photon equivalent and RMS is 10%. The velocity of scintillation light passing in scintillator and WLS fiber is 5.2 cm/ns and the time resolution is 1.79 ns. It is confirmed that scintillation is

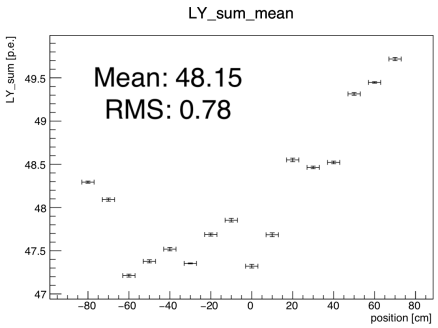

Fig. 3.22: Correlation between LY_sum and hit position. X axis is center position of trigger and Y axis is sum of light yield of both sides.

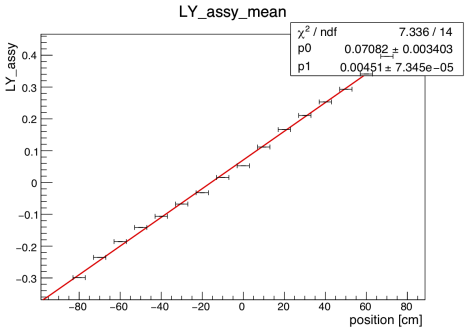

Fig. 3.23: Correlation between LY_assy and hit position. X axis is center position of trigger and Y axis is asymmetry of light yield of both sides.

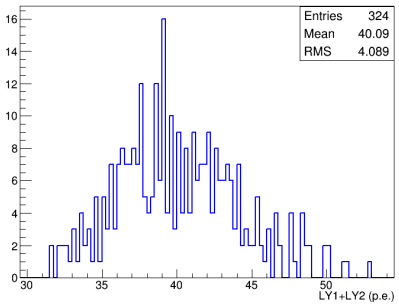

Fig. 3.24: LY_sum distribution for 324 scintillators with the position of trigger fixed at center of scintillator.

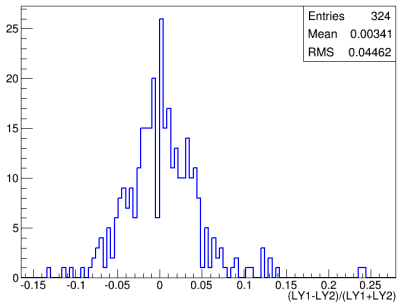

Fig. 3.25: LY_assy distribution for 324 scintillators with the position of trigger fixed at center of scintillator.

decayed according to exponential function and the asymmetry between left and right readout is proportional to hit position. If hit position is estimated by the asymmetry, the position resolution is about 40 cm.

4 Development of electronics and data acquisition system

The electronics of the WAGASCI experiment, including the whole DAQ system, has been developed at Laboratoire Leprince-Ringuet (LLR) of l ' Ecole polytechnique. The front-end and back-end board based on SPIROC chips have been developed. In this chapter, the development of the front-end board with SPIROC2D and developed data acquisition system used in SideMRDs, which are almost same as that used in central detectors, are described.

4.1 Requirements

Requirements from WAGASCI experiment for electronics are:

- Charge measurement for track reconstruction, energy reconstruction and particle identification.
- Hit timing measurement for hit position estimation and neutrino event selection.
- Stable control of 160 channels of MPPCs.

The typical light yield is about 20 p.e. from scintillator mass test. Charge measurement up to about a hundred p.e. is required for electronics. Charge resolution to classify a peak of MPPC is also required.

T2K neutrino beam structure is shown in Figure 4.1. Neutrino beam bunch comes 8 times every 581 ns and the width of a bunch is 58 ns. It is minimum requirement to distinguish two beam bunches. In order to measure the direction of particles, more precise hit timing measurement, about 1 ns, is required.

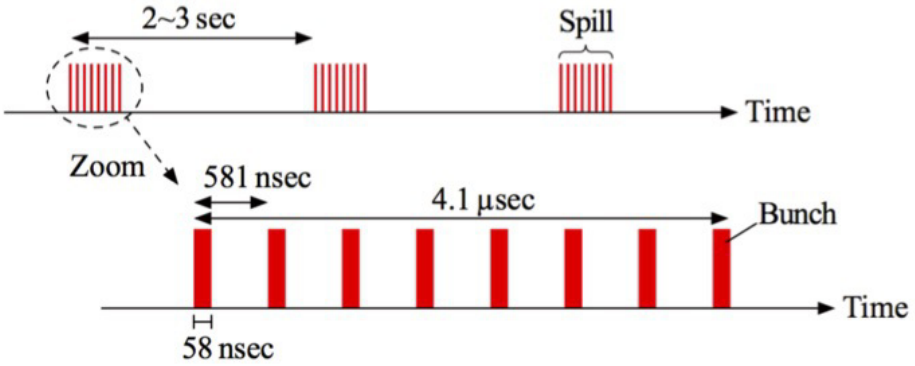

Fig. 4.1: Bunch structure of T2K neutrino beam.

4.2 Design of electronics

The boards in the SideMRD electronics are described as follows:

- ASU (Active Sensor Unit)

  The ASU board, as shown in Figure 4.2, has a SPIROC2D chip, and is connected to several dozens of MPPCs through Single MPPC Board. It also has connections to an Interface board and another ASU via two 50-pin connectors.

- Single MPPC Board

  The Single MPPC Board, as shown in Figure 4.3, has connections to 32 MPPCs via coaxial cable. An MPPC is mounted on a printed circuit board directly. It also has connection to an ASU board via 50 channel flat cable.

- Interface

  The interface board, as shown in Figure 4.4, has connections to four ASUs and a DIF, and transfers signals between the DIF and the four ASUs in parallel. It also has a NIM connection for MPPC bias voltage supply, which is sent to MPPCs through ASUs. Power for the chips such as FPGA on DIF and SPIROC on ASU is also provided through this board.

- DIF (Detector InterFace)

  The DIF board, as shown in Figure 4.5, has an FPGA, which controls the SPIROC chips. It sends DAQ signals and configuration data to the chips, and receives response signals and output data from the chips through the Interface board. The firmware is controlled by the GDCC board through an HDMI connection.

- GDCC (Giga Data Concentrator Card)

  The GDCC board, as shown in Figure 4.6,, has HDMI connections of seven DIFs. It has an FPGA, which only works as signal transfer between an Ethernet to a DAQ PC and HDMIs to DIFs. The GDCC board can also function as CCC mode if the corresponding firmware is loaded on the FPGA.

- CCC (Clock and Control Card)

  The CCC board provides all the GDCCs connected to it with clock signals and fast controls.

The whole system of the SideMRD electronics is shown in Figure 4.7. Total 4 DIFs are used in parallel and a DIF is connected with 3 ASUs which have 80 channels to MPPCs. CCC gets the external trigger signal and pass the clock signal to each DIFs. The system is planned to be integrated into WAGASCI by using same GDCC and CCC. The validation will be done.

Fig. 4.2: Picture of ASU board with SPIROC2D.

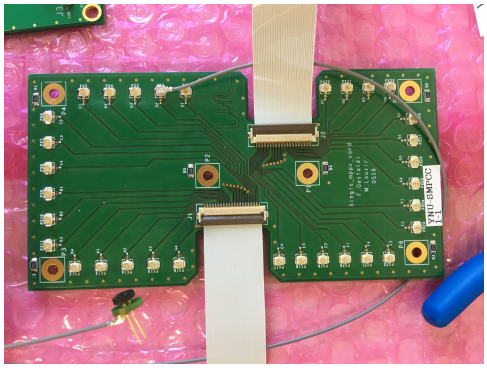

Fig. 4.3: Picture of Single MPPC Board connected with a MPPC via a printed circuit board and a coaxial cable.

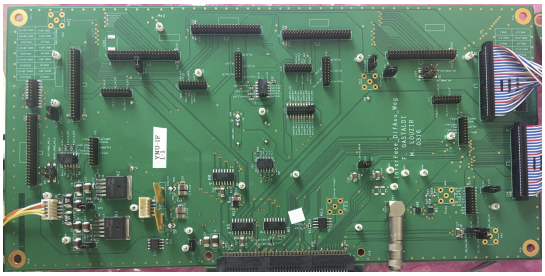

Fig. 4.4: Picture of Interface board.

Fig. 4.5: Picture of DIF board.

4.3 SPIROC2

SPIROC is designed as front-end electronics for an ILC prototype hadronic calorimeter with SiPM readout. It has been developed to satisfy requirements such as large dynamic range, low noise, low energy consumption, high precision and large number of readout channels. Table 4.1 shows the basic characteristics of SPIROC. SPIROC2 is the second iteration which fixes the problems observed on the first version (SPIROC1).

The SPIROC2D chip is a new version of SPIROC2. The former version, SPIROC2B, had wrong behavior on the TDC ramp because of the large dead time due to the multiplexer. In SPIROC2D this problem is solved by implementing a rising and a falling ramp. Although their configurations are done with different numbers of bits, the number and assignment of the pins are compatible between the two versions.

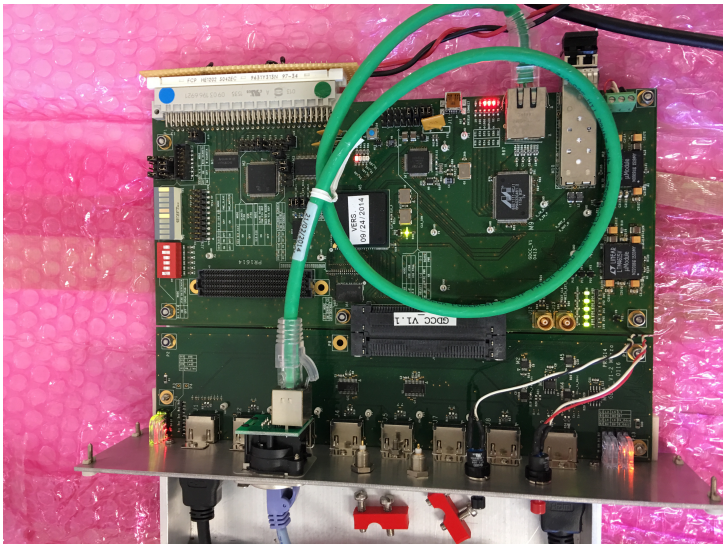

Fig. 4.6: Picture of GDCC board.

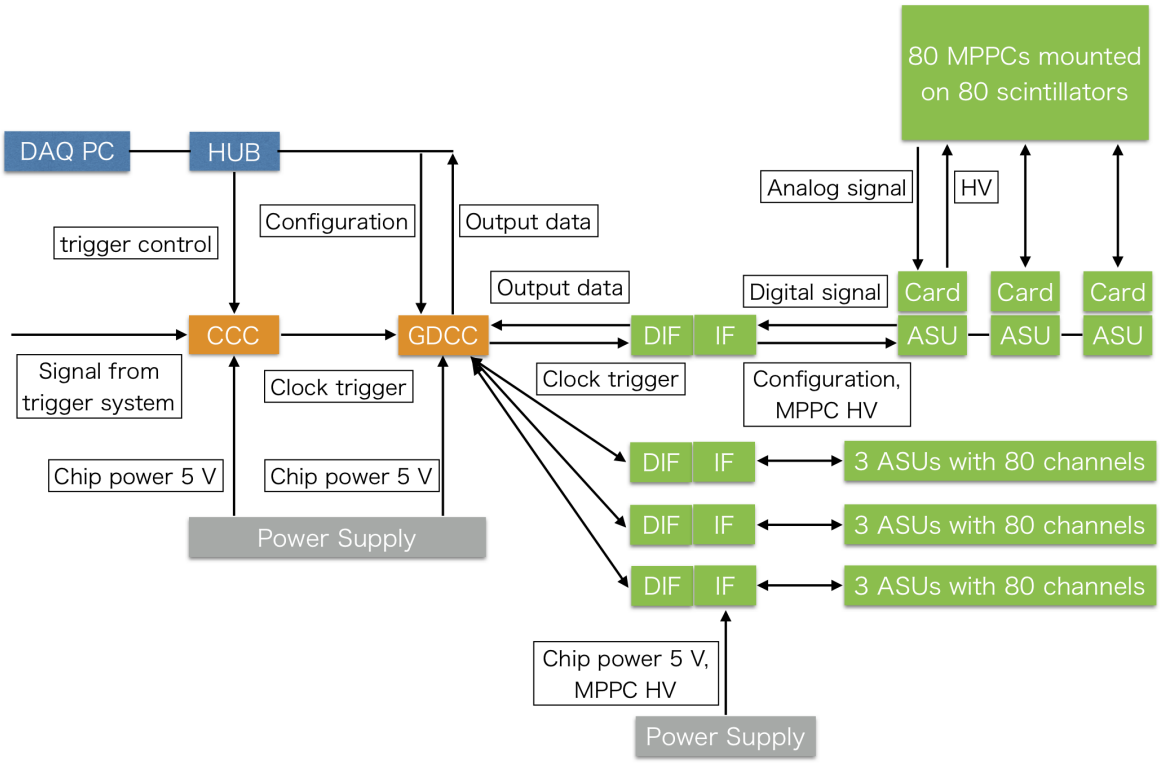

Fig. 4.7: The Block diagram of the whole system of the SideMRD electronics.

Characteristics	Specification
Standard package	CQFP240
Operation voltage	5 V/3.3 V
Power consumption	25 μW per channel (in idle mode)
SiPM gain adjustment	Internal input 8-bit DAC (0-5 V)
Bi-gain / 12-bit ADC	1 p.e. to 2,000 p.e.
Variable shaping time	50 ns to 100 ns
Noise (energy)	pe/noise ratio : 11
TDC	-100 ps step
Noise (time)	pe/noise ratio on trigger channel : 24
Fast shaper	-15 ns shaping time
Auto-trigger	on 1/2 p.e.

Table 4.1: SPIROC main characteristics

4.3.1 Analog part

Figure 4.8 shows the block diagram of the analog parts in SPIROC2. SPIROC2 has identical 36 analog processing circuit and can control bias voltage to MPPC by 8-bit InputDAC, gain by 6-bit variable capacitor and threshold by 4-bit threshold adjustment for 36 channels independently. An analog memory array with depth of 16, named column, is embedded on the chip and used to store charge and timing information. A 12-bit Wilkinson ADC digitizes the information and sends the data to 4 kbytes RAM.

In case that a incoming signal is lower than a defined value, the signal is amplified by High gain Preamplifier, while in case that the signal is higher, the signal is amplified by Low gain preamplifier to keep the signal in the range of ADC. The signal is shaped by Fast Shaper and NIM clock is generated by Discriminator when the signal is over the threshold. The timing information of the NIM signal is stored in 16 columns in turns. The amplified signal is also shaped by Slow Shaper. The height of the slow-shaped signal is held at the timing that the delayed NIM signal comes, and stored in 16 columns in series. In case that a channel gets a signal over the threshold, all channels store the charge information of each channels at the same time. Whether a measured signal is over the threshold or not is also recorded as hit information.

4.3.2 Digital part

SPIROC is equipped with the digital part in the chip. Its readout process has four phases:

1. Idle phase

   In the idle phase, a capture window is open at the first empty data column. This phase saves the power consumption when any other processes are not running.

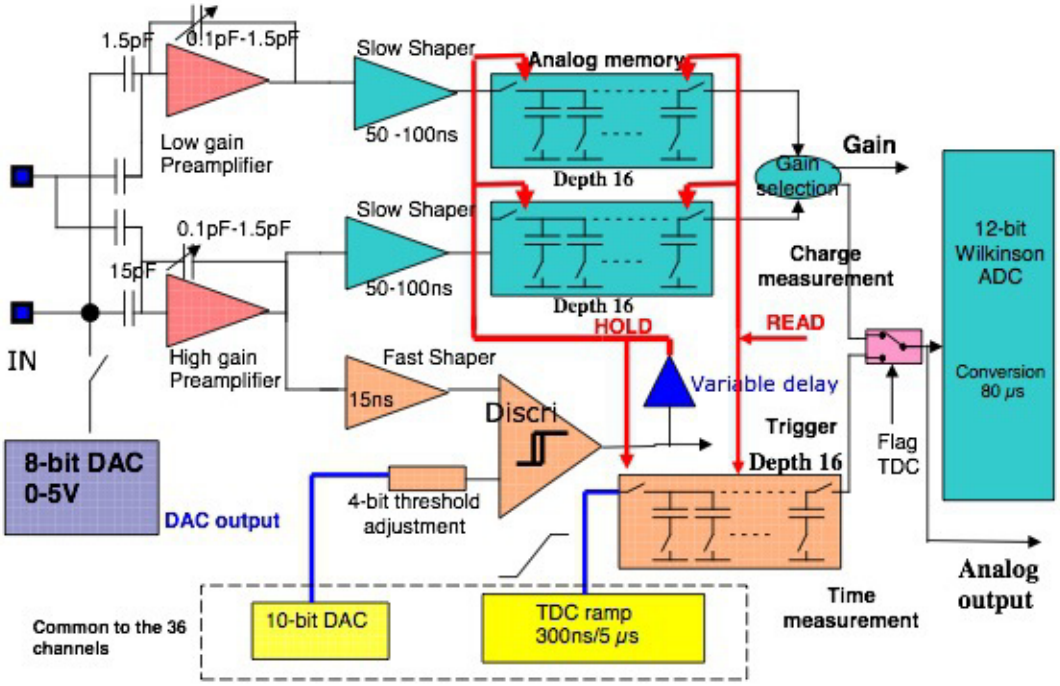

Fig. 4.8: The block diagram of the analog part in SPIROC2.

2. Acquisition phase

   Figure 4.9 shows the diagram of the digital parts relevant to the acquisition phase. At the timing of trigger, charge and timing information are stored in the analog memory and saved in the current data column. When the capture windows are closed, the data column moves to the next at the same time for all the channels. A "bunch crossing", which is a coarse time flag for the triggers, also shifts the column to the next if there is no trigger before the bunch crossing. An external signal is optionally able to erase data in the current column.

3. Conversion phase

   All the 36 charge and 36 timing in the analog memory are sequentially converted at an ADC with using ramp signals, and the digital data are stored in the 4 kbytes SRAM.

4. Readout phase

   The stored data are transferred out of the chip with a single line, and the analog memory becomes empty after all the data are transferred. If more than one chip are controlled together, a token enabling the data transfer is sent to the next chip when the data transfer for the first chip is done. The maximum number of chips which can be readout through on serial link is 256.

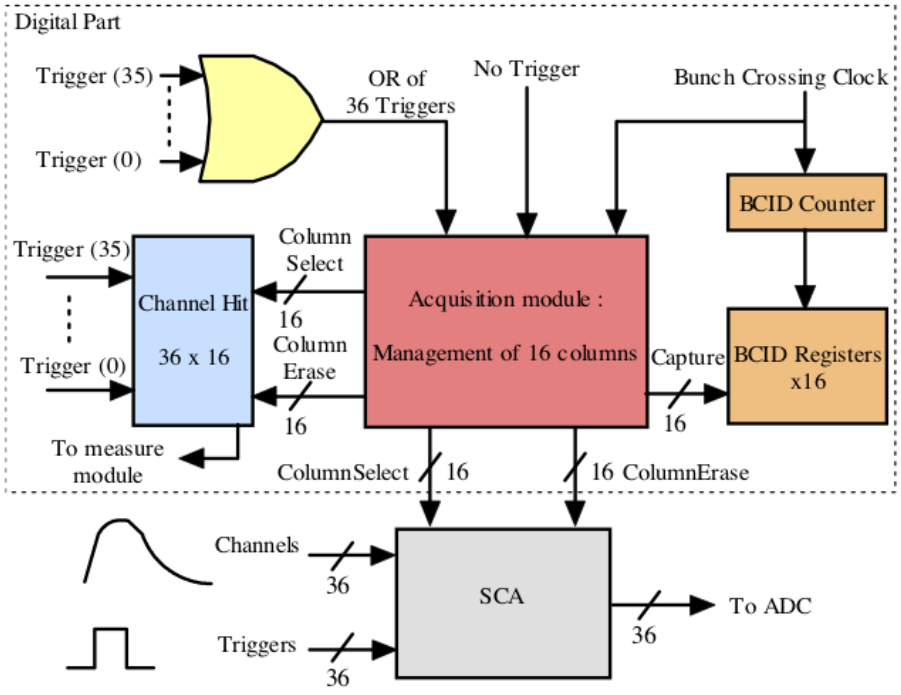

Fig. 4.9: The block diagram of the digital part in SPIROC2.

4.4 Link between DAQ and SPIROC

Sequence of phases on the digital parts in SPIROC is controlled by signals from DAQ. SPIROC provides response signals for DAQ. Signals sent from DAQ to SPIROC are start acquisition, start conversion, and start readout, as well as reset and clocks. Signals from SPIROC to DAQ are chip saturation and end readout. Figure 4.10 shows chronogram of the DAQ signals for each case with all the 16 memories full or not full. The DAQ signals control the process in the following order.

1. Reset

   All the digital part are reset first.

2. Start acquisition

   The acquisition phase starts and is maintained during this signal.

3. Chip saturation

   When all the 16 memories become full, the acquisition phase finishes and then the conversion phase starts. When the memories do not become full during the data taking period, the acquisition phase ends and the chip saturation signal is induced to start the conversion phase. This chip saturation signal is maintained during the conversion phase.

4. Start conversion
5. Start readout

   As the conversion phase ends with the trailing edge of the chip saturation signal, the readout phase starts with the start readout signal.

6. End readout

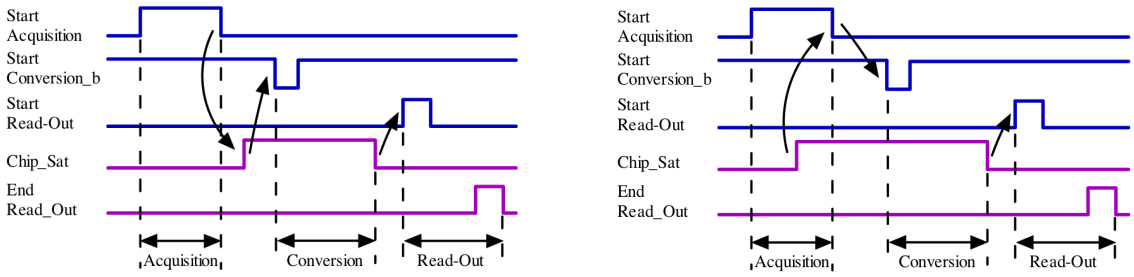

Fig. 4.10: The chronogram of the DAQ signal in case that the chip does not get full (left) and in case that the chip gets full (right).

4.5 Data structure

SPIROC2 data stream is shown in Figure 4.11. The charge and time information converted by a 12-bit Wilkinson ADC are stored with 1-bit hit information and 1-bit gain select information. In order to acquire charge information with large dynamic range and to save the data size, SPIROC2 adopts two different magnification preamplifier, high gain preamplifier and low gain preamplifier, and the switch of them which enables automatic shift from high gain to low gain when the amplitude of signal is very high. The 1-bit gain select information is the flag of this switch. The 1-bit hit information indicates whether the signal of the corresponding channel is triggered by the threshold or not. The charge and time information are stored 36-channels together and bunch crossing ID follows it. In the end of data stream, chipID is stored.

SPIROC2 data stream is packaged chip by chip with the DIF header and trailer including 8-bit DIF identifying chipID, which is different from chipID of SPIROC2. The chip data stream is packaged with the GDCC header and trailer including 32-bit GDCC counting acquisition gate number. Above of all, the beam trigger information which contains lower 16-bit beam trigger number information and 8-bit trigger mode are stored. The highest bit of 8-bit trigger mode indicates that the acquisition gate is generated by external trigger or internal periodic trigger.

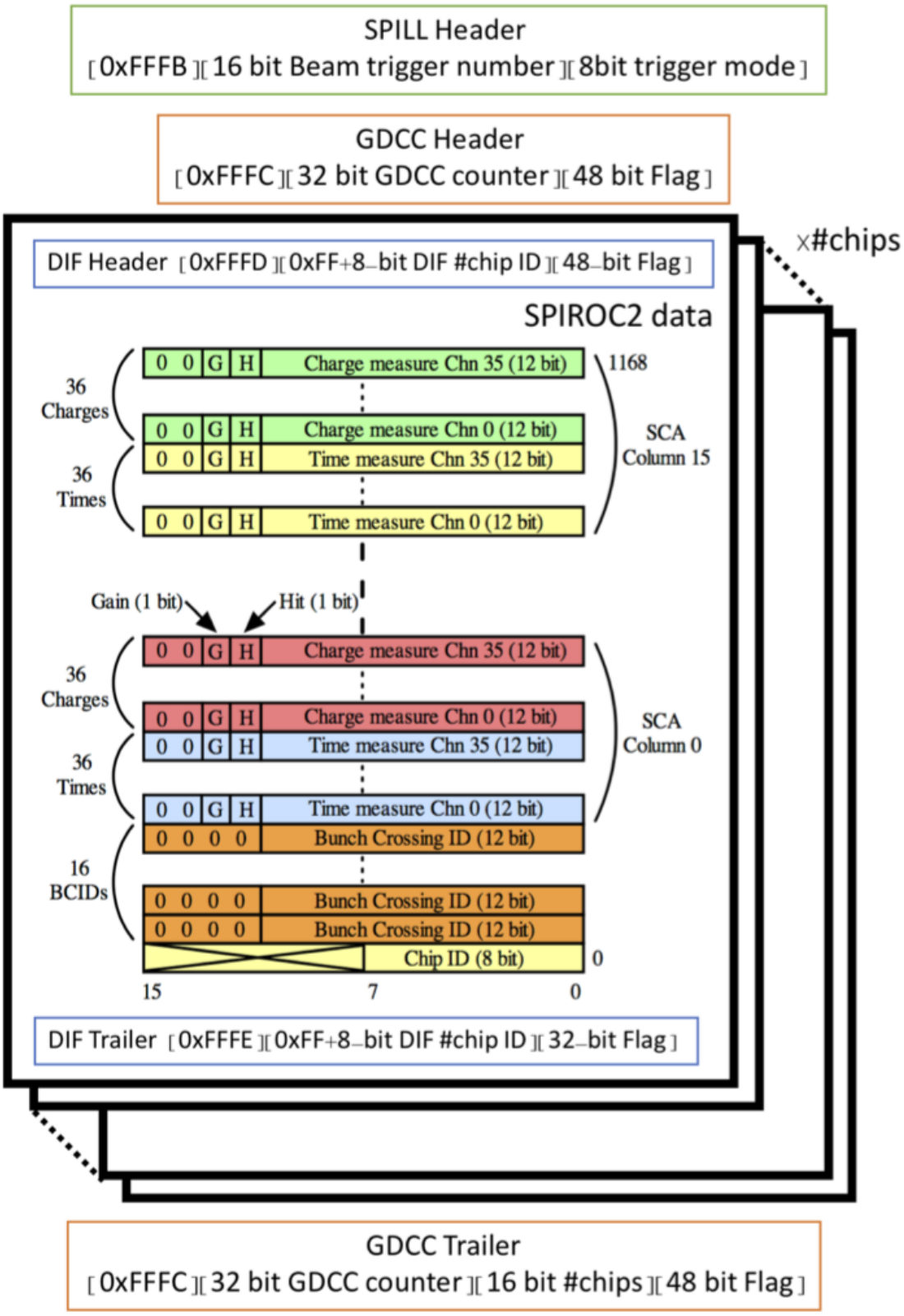

Fig. 4.11: Data structure of SPIROC2.

4.6 Test measurement

The test measurement of the board based on SPIROC2D is done in simple conditions. The purpose of the test measurement is to understand the behavior of the board, improve it and confirm that the board satisfies the experiment requirements.

4.6.1 Setup

The setup is shown in Figure 4.12. Only one ASU based on SPIROC2D and one single MPPC are used. An MPPC and a LED are in the black box and the distance is fixed.

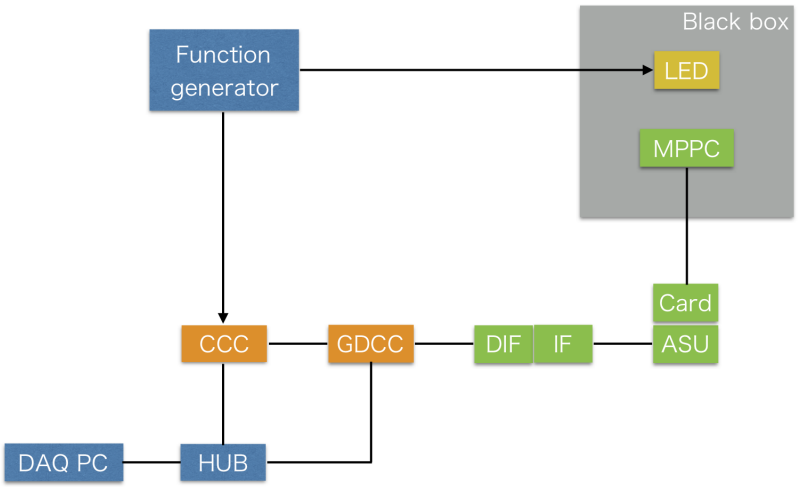

Fig. 4.12: Data structure of SPIROC2.

4.6.2 ADC distribution

Figure 4.13 shows ADC distribution of SPIROC with LED light injection. Peaks corresponding to each p.e. are observed clearly. ADC distribution of each analog memory is shown in Figure 4.14. The peaks are also seen clearly in all analog memories.

Stability of gain and pedestal among 16 depth analog memory is also checked. Gain is calculated by measuring the distance of two neighboring peaks, same as Equation 3.3 as shown in Figure 4.15 and 4.16. Pedestal is obtained by measuring dark noise of MPPC without LED in the same setup as Figure 4.12. Figure 4.17 shows the dark noise event of MPPC and pedestal position is given by fitting it by gaussian. Figure 4.18 shows gain and pedestal of each analog memory.

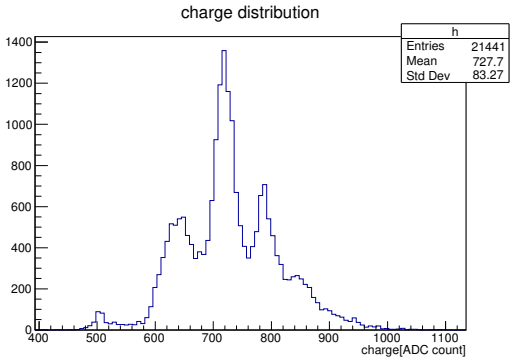

Fig. 4.13: ADC distribution with LED light injection.

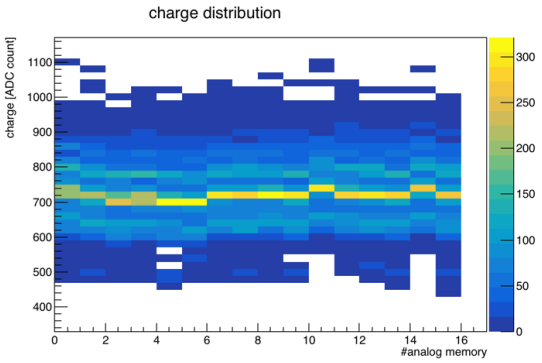

Fig. 4.14: ADC distribution of each memory with LED light injection. X axis is the number of analog memories and Y axis is the ADC distribution.

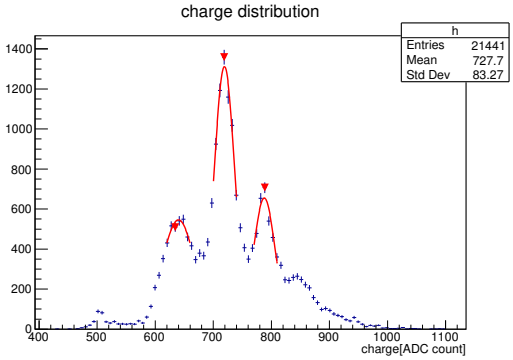

Fig. 4.15: Fitting of charge distribution. Each peak is fitted by gaussian.

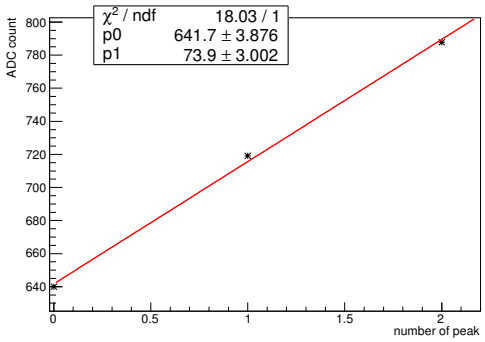

Fig. 4.16: Linear fitting of mean peak position corresponding to each p.e..

4.6.3 InputDAC

Bias voltage to an MPPC varies by changing InputDAC value. It means that gain of MPPC is variable. Figure 4.19 shows the correlation between gain and InputDAC when bias voltage is 56.0 V and PreampDAC is 53. It shows that gain is proportional to InputDAC.

The correlation between gain and bias voltage is also measured when InputDAC is set to 70 and PreampDAC is 53. Figure 4.20 shows the correlation. Gain is also proportional to bias voltage.

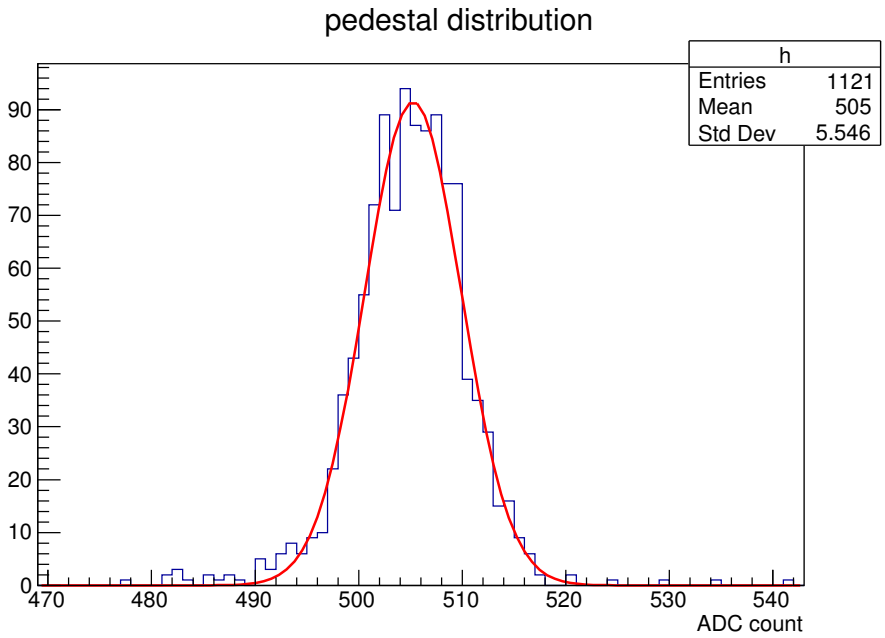

Fig. 4.17: ADC distribution of MPPC dark noise. Pedestal value is obtained by fitting the peak by gaussian.

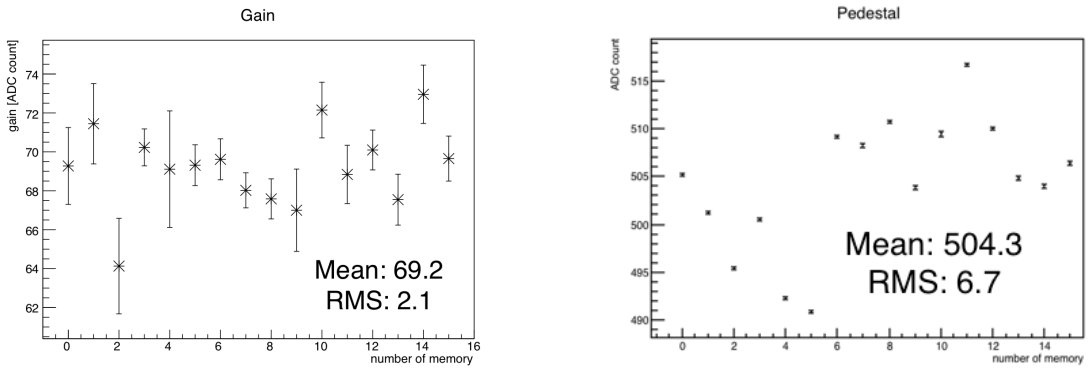

Fig. 4.18: Gain distribution (left) and pedestal distribution (right) of each memory. X axis is the number of analog memories and Y axis is the ADC count of gain and pedestal position.

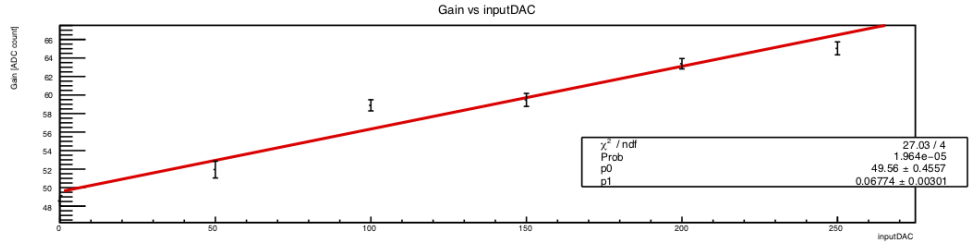

Fig. 4.19: Correlation between gain and InputDAC. X axis is InputDAC value and Y axis is gain.

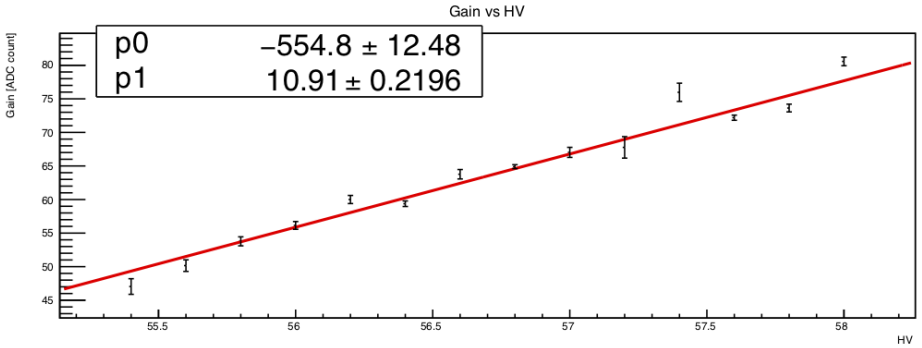

Fig. 4.20: Correlation between gain and bias voltage. X axis is bias voltage and Y axis is gain.

4.6.4 PreampDAC

The capacitance of preamp varies by changing PreampDAC value. That's why ADC count of gain is variable. Figure 4.21 shows the correlation between gain and PreampDAC when bias voltage is 55.0 V and InputDAC is 70. The correlation function is given as following equation:

$$Gain = \frac{1212 \pm 22}{74.67 \pm 0.38 - PreampDAC}. \tag{4.1}$$

The equation suggests that gain is proportional to the impedance of the preamp capacitor, $1/\omega C$, where ω is the angular frequency and C is the capacitance.

4.6.5 ThresholdDAC

One of the known issues is that the reference of the comparator in SPIROC2D is wrong as shown in Figure 4.22. Due to this issue, it is only possible to set the discriminator threshold at undershoot. It may make measurement very sensitive to electronics noise. This issue occurs not on a mounting board but on a ASIC chip, so it

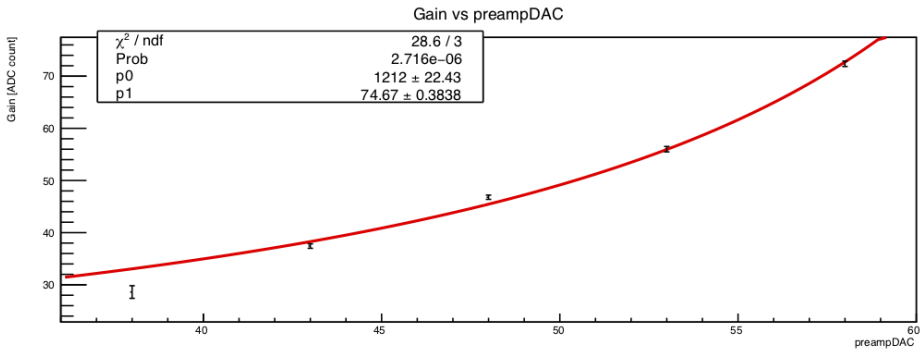

Fig. 4.21: Correlation between gain and PreampDAC. X axis is PreampDAC value and Y axis is gain.

is difficult to fix this issue. It is one of the most important tests to confirm the effect of wrong position of comparator.

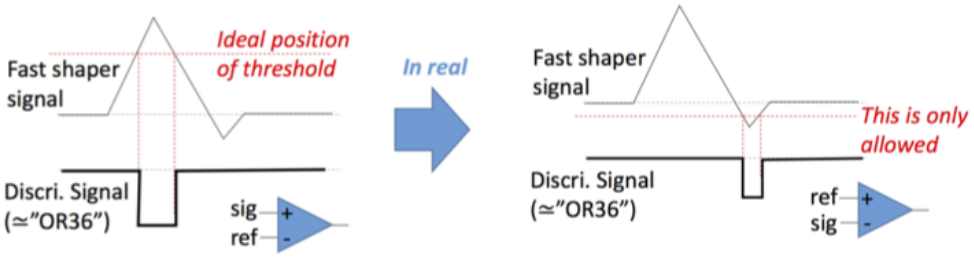

Fig. 4.22: Wrong position of comparator of SPIROC2D. It forces to set the discriminator threshold at undershoot.

In order to confirm the effect, dark noise rate of a MPPC is scanned with changing ThresholdDAC value. SPIROC does not have a counter and the time opening a acquisition gate is variable due to random timing of saturation of 16 depth analog memory, so dark noise cannot be measured by the same way as Equation 3.4. The dark noise rate is measured by using BCID information. Figure 4.23 shows a typical plot of BCID of dark noise. The number of entires of each bins basically become constant due to randomness of dark noise, but the tail of curve is seen because acquisition gate is closed when analog memory gets full. The dark noise rate is calculated as follows:

the probability that dark noise comes in a BCID bin of a spill, P_1, is calculated as

$$P_1 = \frac{A}{N} \tag{4.2}$$

$$= \sum_{i>0}^{\infty} P_0^i = \frac{P_0}{1 - P_0} \tag{4.3}$$

where N is the number of total acquisition gates, A is the number of entries of a bin and P_0 is the probability that dark noise comes once in a BCID bin. A is obtained by fitting plateau range of BCID plot with constant. Dark noise rate is calculated as

$$Dark\ noise\ rate = \frac{P_0}{T} = \frac{P_1}{1 + P_1} \times \frac{1}{T} \tag{4.4}$$

$$= \frac{A}{A + N} \times \frac{1}{T} \tag{4.5}$$

where T is the time corresponding to a BCID bin, which is set to 580 ns corresponding to a period of neutrino beam bunch.

Figure 4.24 shows the result of the scanning using above method. It is seen that the typical curve of MPPC noise rate has some plateau ranges. Each plateau range correspond to the threshold level for each photo electron equivalent level, and plateau ranges from 1 p.e. to 3 p.e. are clearly seen. It means that threshold can be set from 1p.e. although position of comparator is wrong. The signal height corresponding to each p.e. level is depending on the gain, therefore the threshold level is depending on the gain. It means that the precise tuning of threshold according to the gain is needed.

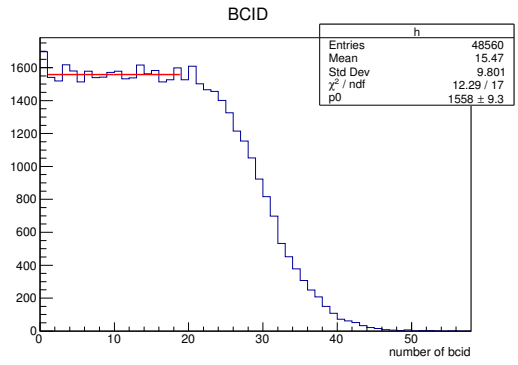

Fig. 4.23: BCID plot given by measuring dark noise. X axis is BCID and Y axis is the number of entry.

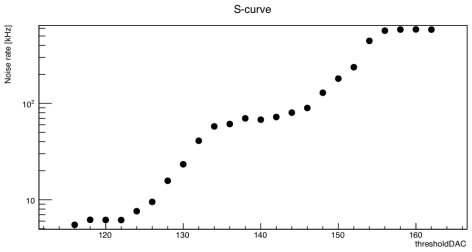

Fig. 4.24: S-curve of noise rate. X axis is ThresholdDAC value and Y axis is the noise rate.

4.6.6 BCID distribution

Figure 4.25 shows BCID distribution obtained by measuring periodic light injection of LED. The period of LED is 5,800 ns corresponding to 10 BCIDs. BCID distribution

have peaks every 10 BCIDs ideally, but no peak is seen. This is due to bad synchronization between BCID clock and acquisition gate. The issue is expected to be improved after updating DIF firmware. The updating work is done and the jitter of timing is improved to ∼40 ns.

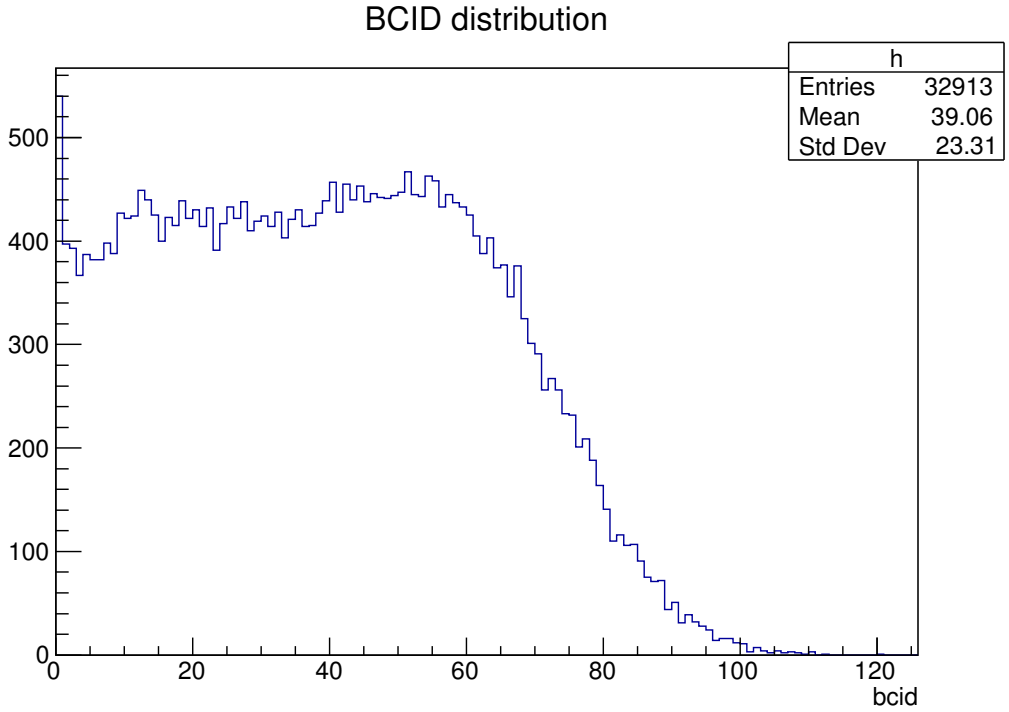

Fig. 4.25: BCID distribution with LED light injection.

4.6.7 TDC distribution

TDC has ramp structure. TDC ramp has different slope according to whether BCID is odd or even. When LED light synchronized with acquisition gate is used, hit timing becomes constant. By measuring the TDC count by adding delay to LED, TDC ramp structure appears and the slope is obtained. Figure 4.26 shows the correlation between time and TDC count. The equation is obtained as

$$TDC\ count = (5.822 \pm 0.006) \times T - 92 \pm 3, \tag{4.6}$$

where T is relative time [ns]. Hit timing distribution is obtained from TDC distribution by using above equation as shown in Figure 4.27. The timing distribution has two peaks. Assuming one peak is correct, the time resolution is obtained as the RMS, 0.45 ns.

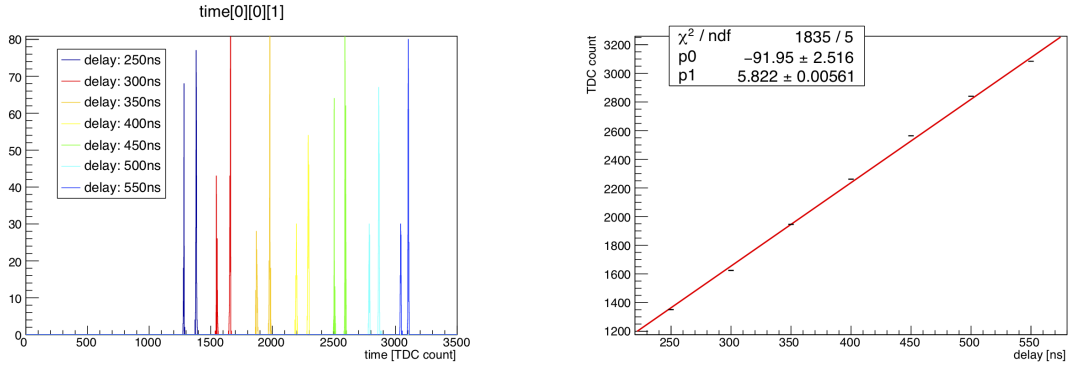

Fig. 4.26: TDC shifted as delay of hit timing (left) and the correlation between TDC count and delay time (right).

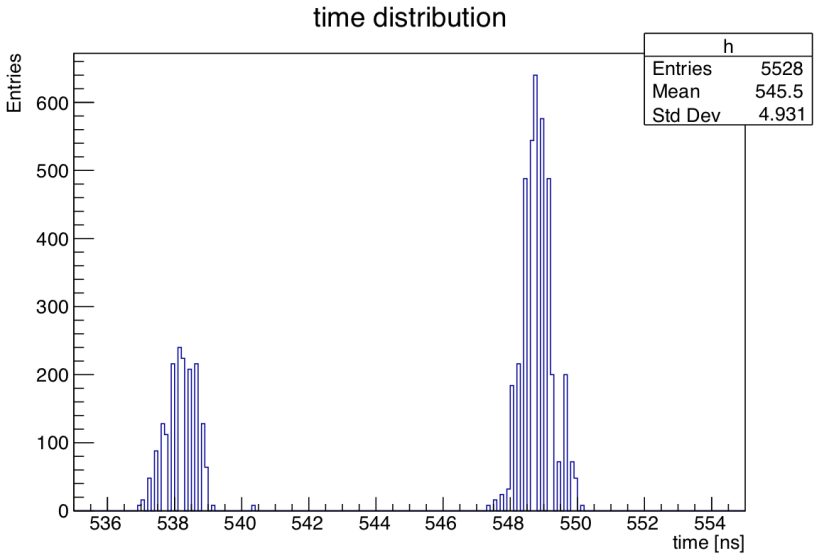

Fig. 4.27: Hit timing distribution with periodic LED light injection.

5 Detector construction

SideMRD modules were constructed from December 2017 to June 2018 in YNU. First SideMRD was constructed from December 2017 to March 2018, and Second one was from April to June 2018. Construction process is listed as below.

1. Constructing iron structure
2. Inserting scintillators
3. Mounting electronics

5.1 Constructing iron structure

Figure 5.1 is the schematic of iron structure of SideMRD. The iron structure is constructed by Nichirei-Seiki as shown in Figure 5.2.

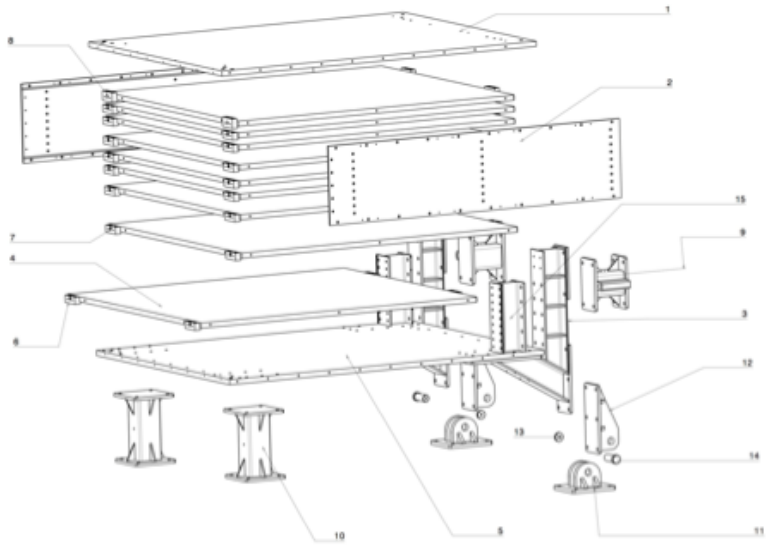

Fig. 5.1: A schematic view of SideMRD iron structure.

5.2 Inserting scintillators

The 8 scintillators are inserted between iron layers and total 80 scintillators are required for a SideMRD module. The gap between iron layers is 13 mm, while the sickness of a scintillator is 7 mm. In order to fill the gap and fix the scintillator, a scintillator is attached with four sponge rubbers as shown in Figure 5.3. The size of

Fig. 5.2: States of SideMRD iron structure construction.

a rubber is 3×20×1800 mm^3. The scintillator attached rubbers is also covered with Tyvek sheet to shield the scintillator and WLS fiber and make insertion easy due to friction of the rubber as shown in Figure 5.4. Figure 5.5 shows the SideMRD after scintillator installation.

5.3 Mounting electronics

Electronics are mounted on two sides of a module independently, called Top and Bottom. Figure 5.6 shows the Top view after mounting electronics. A DIF attached with a Interface and three ASU boards attached with three Single MPPC Board are mounted for each side. 80 single MPPCs are connected with each channels of three ASUs. The electronics are connected with backend electronics through a patch panel as shown in Figure 5.7. Figure 5.8 shows the Top view after mounting a aluminum cover attached with a patch panel and cooling module.

Fig. 5.3: A view of sponge rubber (left) and scintillators attached with the rubbers (right).

Fig. 5.4: A scintillator covered with Tyvek sheet.

Fig. 5.5: Top view of SideMRD after installation of 80 scintillators.

5.4 Test with cosmic ray

The performance of two modules is tested after construction by measuring light yield with cosmic ray. The measurement setup is same as Figure 4.7. The parameters of electronics are set as follows: bias voltage to MPPCs is 58.0 V, InputDAC is 41 for all channels, PreampDAC is 53 for all channels, and ThresholdDAC is 120 according to

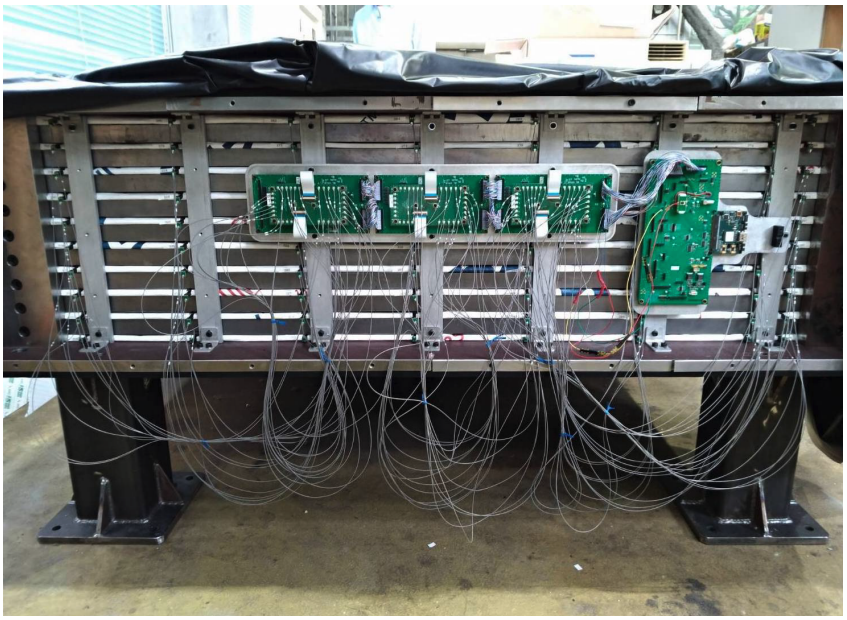

Fig. 5.6: Top view after mounting electronics.

Fig. 5.7: A schematic view of patch panel.

1.5 p.e. level. Figure 5.9 and 5.10 show the light yield distribution for each sides of two modules, 1st and 2nd. Mean of light yield for each side is obtained about 20 p.e..

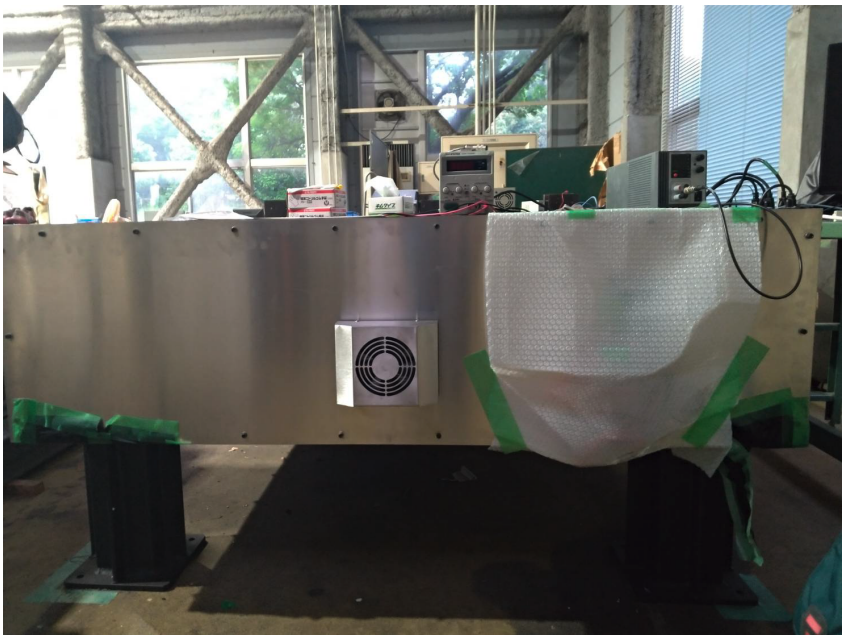

Fig. 5.8: Top view after mounting aluminum cover.

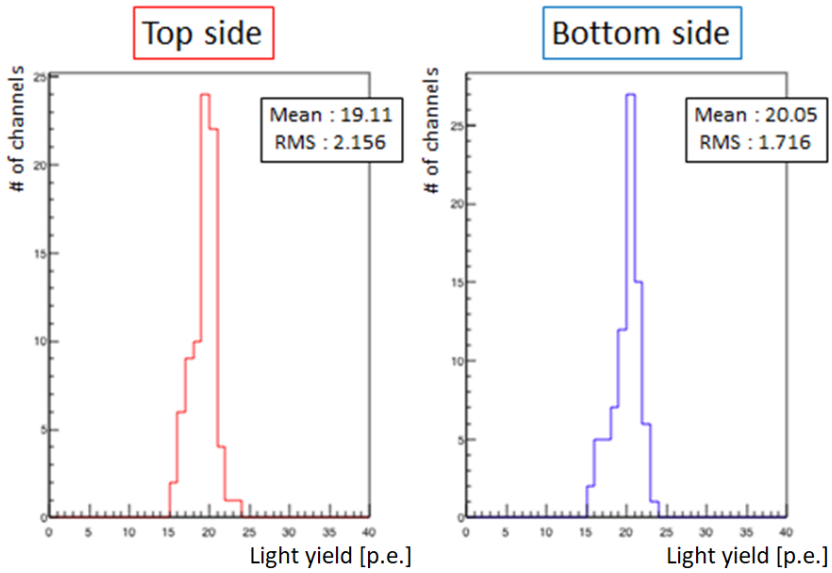

Fig. 5.9: Light yield distribution of 80 scintillators for Top (left) and Bottom (right) side of first module.

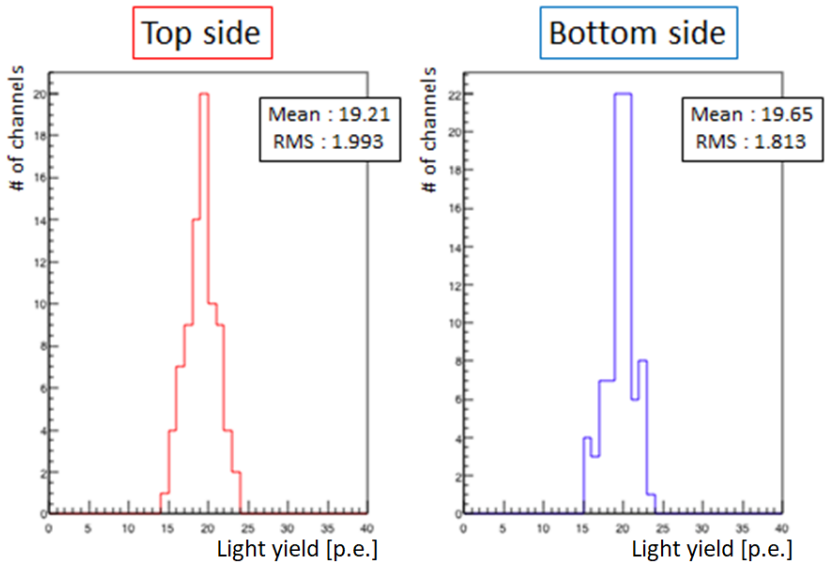

Fig. 5.10: Light yield distribution of 80 scintillators for Top (left) and Bottom (right) side of second module.

6 Commissioning with cosmic ray

SideMRDs were transported from YNU to Neutrino Monitor Building in J-PARC at June 2018 as shown in Figure 6.1. The performance of SideMRDs are evaluated after the transportation.

Fig. 6.1: A view of SideMRDs at Neutrino Monitor Building in J-PARC.

6.1 Track reconstruction

Track reconstruction method for selection of muon events from hit information is described. The track reconstruction method consists of 2 steps, two-dimensional and three-dimensional reconstruction. Charged particles except muon cannot pass through the iron plates due to large energy loss, therefore the reconstructed track is expected to be due to a muon.

6.1.1 2D reconstruction

Two-dimensional reconstruction is done from hit information in both Top and Bottom sides independently. Hit information is selected by the charge information and clustered by time information. The light yield of a hit is required over 4.5 p.e. level to cut noise event. Hits are clustered by BCID and TDC information. In this measure-

ments, DIF firmware was not updated and BCID and TDC had time jitter corresponding to about a BCID bin, so the clustering conditions become coarser than expected. If number of hits having same BCID is three or more, the BCID is defined as clustered BCID. Hits of which difference of BCID is one from a clustered BCID are also classified into the cluster due to time jitter. After updating DIF firmware, the BCID clusters will be classified by TDC information also. After clustering, two-dimensional track is reconstructed using the clusters. Assuming hit position of a scintillator the center of the scintillator and fitting the hit positions by linear, track is reconstructed. Figure 6.2 shows the typical reconstructed track in Top side. Each colored areas show the scintillators.

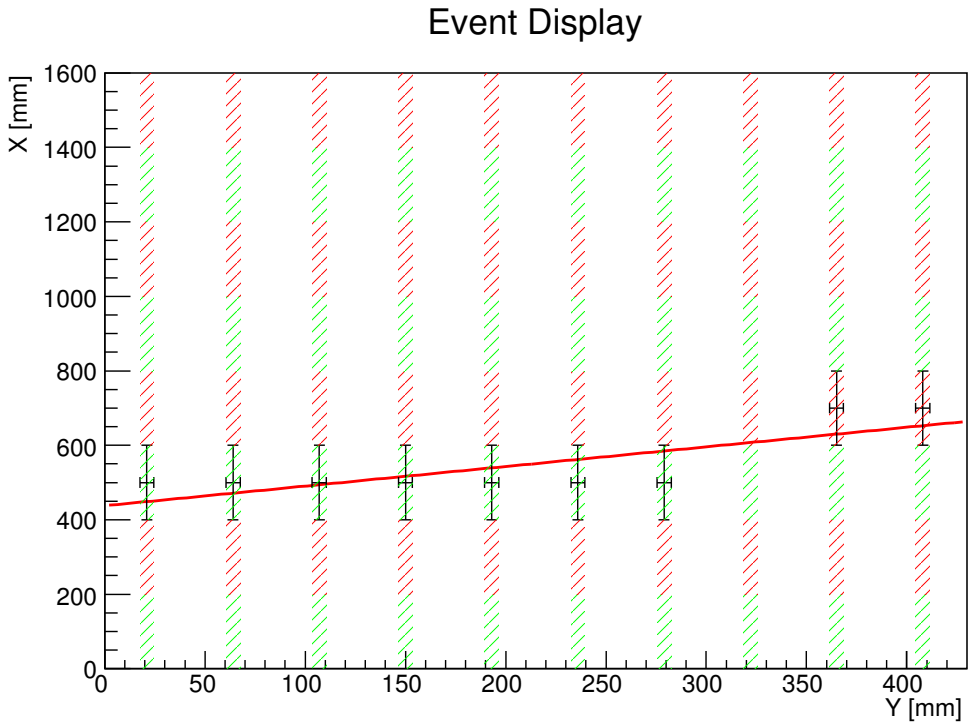

Fig. 6.2: Typical track reconstructed in Top side. Each colored areas are the scintillators.

6.1.2 3D reconstruction

After two-dimensional tracking, the pair of two-dimensional tracks in Top and Bottom side is searched. The conditions of three-dimensional track matching are not optimized, then the procedures are described below: first, BCID clustering is done. Comparing the two-dimensional reconstructed tracks of both side, two tracks in same BCID become candidate of same track. Then track matching is done by comparing the zenith angle and positions of two tracks. Hit position along a scintillator is determined

by using Equation 3.18 and the light yield symmetry of the scintillator. The method is under development in this time, so three-dimensional reconstruction is not applied to the result of this thesis.

6.2 Gain tuning

Figure 6.3 shows gain distribution for channels of each side of modules. The RMS of the gains is about 11%. The gain can be tuned by tuning InputDAC for each channel. The correlation between InputDAC and gain is obtained by measuring charge distribution with cosmic event by changing InputDAC, and gain is tuned to be uniform. Gain distribution after tuning is shown in Figure 6.4. The RMS is about 7%. After installation, gain is also tuned to be uniform by using cosmic trigger.

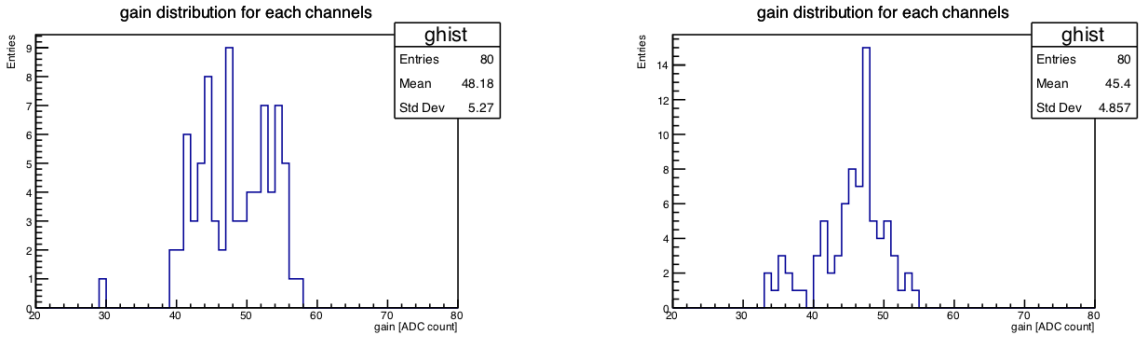

Fig. 6.3: Gain distribution for Top (left) and Bottom (right) side of 1st module.

6.3 Basic distribution

Figure 6.5 shows light yield distribution for all events and for each channels. Average light yield distribution of each channels for each side of modules is shown in Figure 6.6. Zenith angle is obtained by two-dimensional reconstruction for each sides. Figure 6.7 shows zenith angle distribution for each sides, Top and Bottom of two modules. Zenith angle is represented as cosine theta. Path length in a scintillator is also obtained by three-dimensional reconstruction and light yield is corrected by the path length. Figure 6.8 shows light yield distribution after the correction by path length obtained by two-dimensional reconstruction.

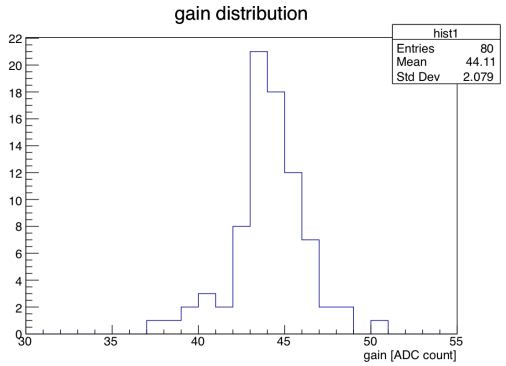

(a) Gain distribution for 1st Top.

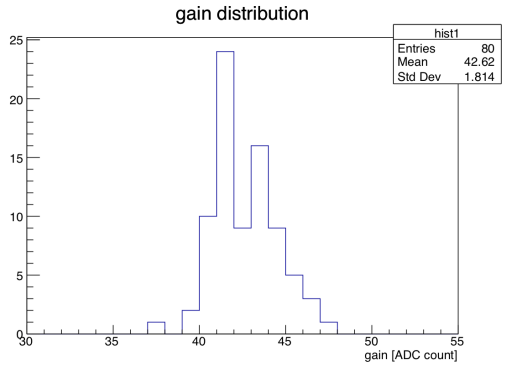

(b) Gain distribution for 1st Bottom.

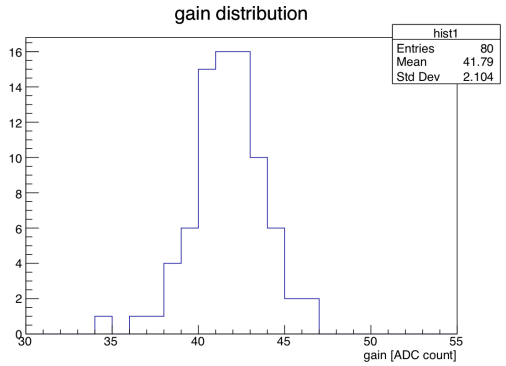

(c) Gain distribution for 2nd Top.

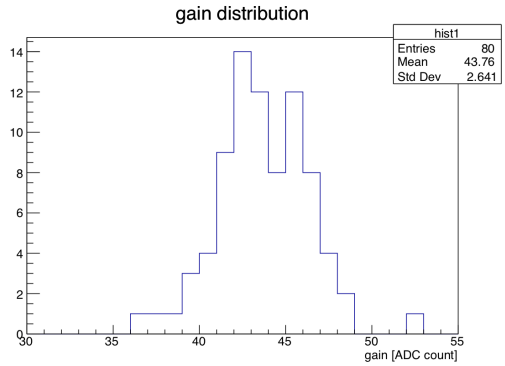

(d) Gain distribution for 2nd Bottom.

Fig. 6.4: Gain distribution after gain tuning for Top and Bottom side of two modules, 1st and 2nd.

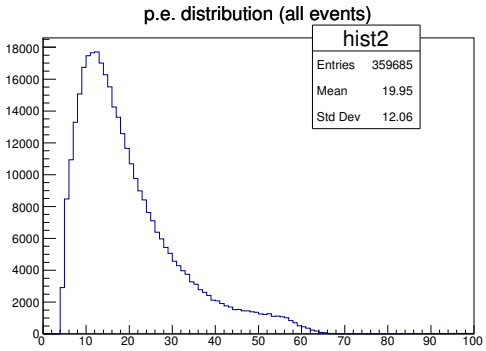

(a) Light yield distribution for 1st Top.

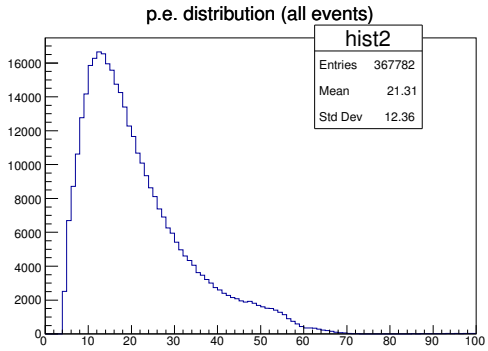

(b) Light yield distribution for 1st Bottom.

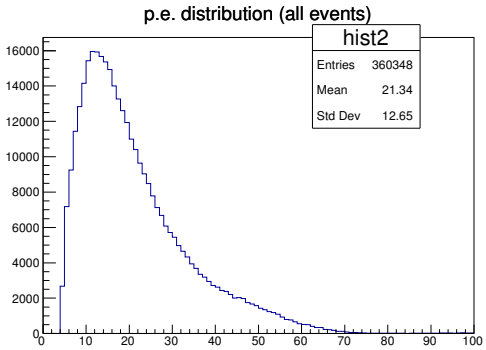

(c) Light yield distribution for 2nd Top.

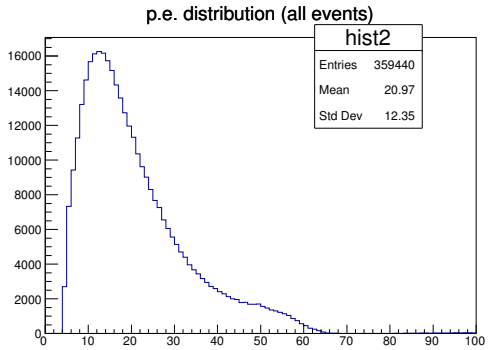

(d) Light yield distribution for 2nd Bottom.

Fig. 6.5: Light yield distribution of all events for Top and Bottom side of two modules, 1st and 2nd.

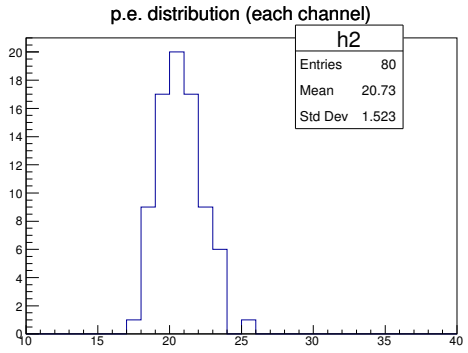

(a) Light yield distribution for 1st Top.

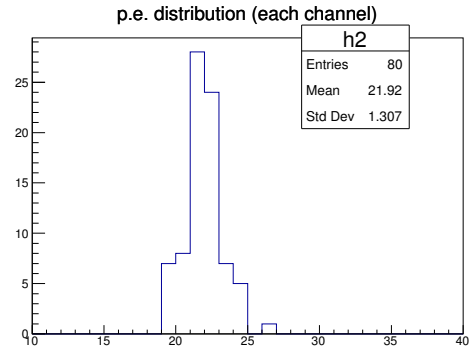

(b) Light yield distribution for 1st Bottom.

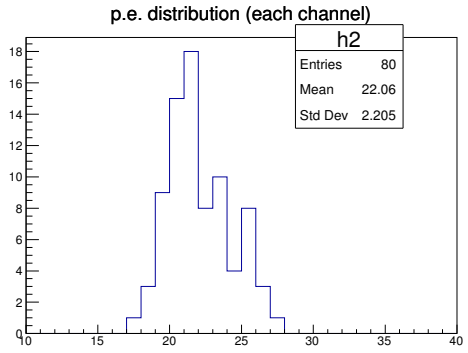

(c) Light yield distribution for 2nd Top.

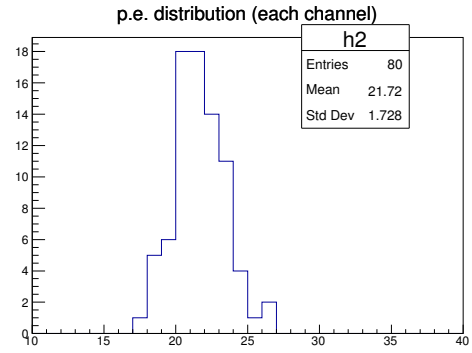

(d) Light yield distribution for 2nd Bottom.

Fig. 6.6: Light yield distribution of 80 channels for Top and Bottom side of two modules, 1st and 2nd.

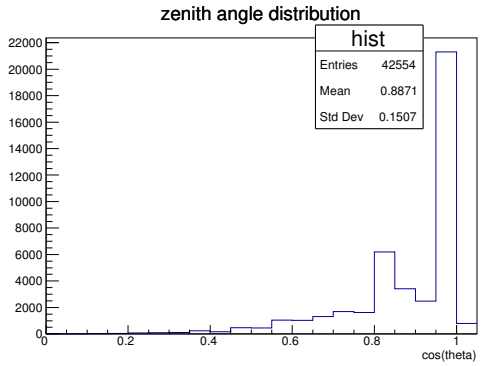

(a) Zenith angle distribution for 1st Top.

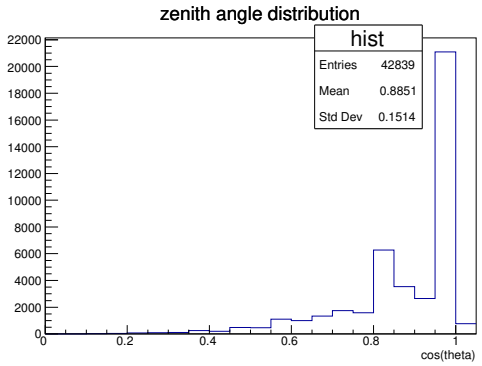

(b) Zenith angle distribution for 1st Bottom.

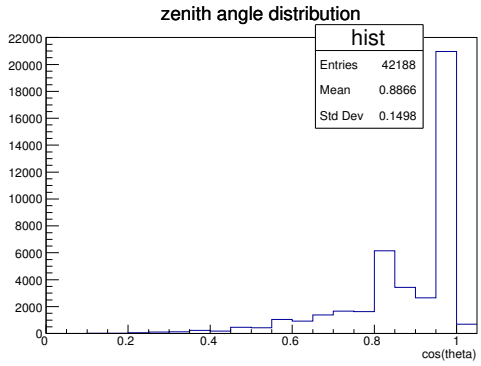

(c) Zenith angle distribution for 2nd Top.

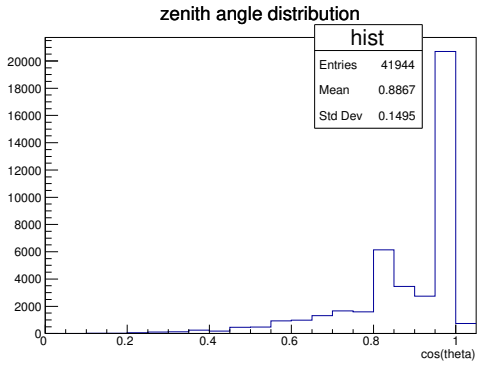

(d) Zenith angle distribution for 2nd Bottom.

Fig. 6.7: Zenith angle distribution of all events for Top and Bottom side of two modules, 1st and 2nd. X axis is zenith angle [cos(theta)] and Y axis is the number of entries.

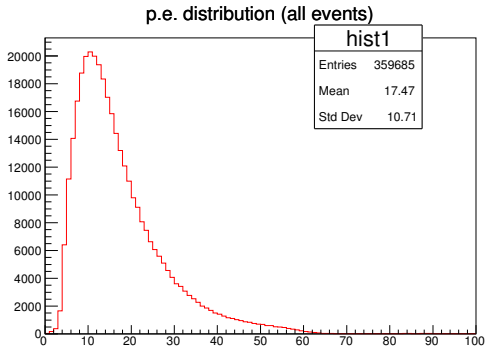

(a) Light yield distribution for 1st Top.

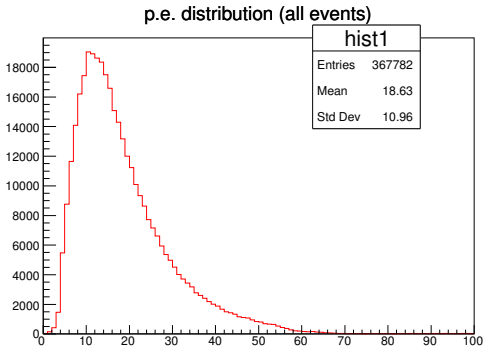

(b) Light yield distribution for 1st Bottom.

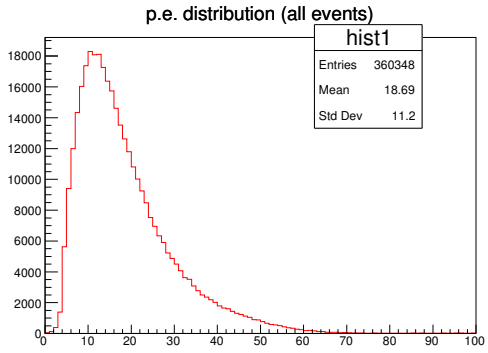

(c) Light yield distribution for 2nd Top.

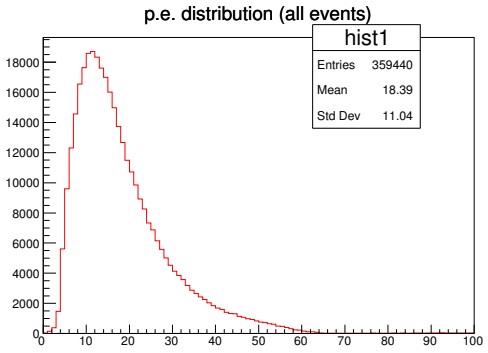

(d) Light yield distribution for 2nd Bottom.

Fig. 6.8: Light yield distribution of all events after correction by path length for Top and Bottom side of two modules, 1st and 2nd.

7 Summary

In order to reduce the current dominant systematic uncertainty in the T2K neutrino oscillation analysis, WAGASCI experiment has been proposed at J-PARC. Its goals are to measure cross-section ratio of water to hydro-carbon and differential cross section of water and hydrocarbon with a large acceptance. In order to select neutrino charged current interaction except background generated out of target detector and reconstruct the momentum of muon generated from neutrino interaction, two muon range detectors, named SideMRDs, are planed to be installed next to the WAGASCI detector.

The performance of scintillators are measured. The scintillator is glued with a WLS fiber in an S-curve shape, attached readout electronics at both sides and the size is $7\times200\times1800$ mm^3. The light yield of cosmic ray is about 20 photon equivalent and the RMS of the light yield is 10%. The velocity of scintillation light passing in scintillator and WLS fiber is 5.2 cm/ns and the time resolution is 1.79 ns. It is confirmed that scintillation is decayed according to exponential function and the asymmetry between left and right readout is proportional to hit position. If hit position is estimated by the asymmetry, the position resolution is about 40 cm.

The performance of the electronics, based on SPIROC2D, is measured. SPIROC2 has 32-channel input and 16-depth analog memory. It is confirmed that the performance of the electronics is stable for each channels and analog memories. Gain is tuned by changing DAC value properly, and then the RMS of gain for channels is improved from 11% to 7%.

Two SideMRDs construction was started at November 2017 and it was finished at June 2018. The performance of SideMRDs are measured and it is confirmed that the light yield obtained with cosmic ray is consistent with scintillator mass test and there is no bad channel. SideMRDs were transported to J-PARC at June 2018. Then the performance was measured and confirmed to be stable.

SideMRDs will be installed by the sides of WAGASCI detector at February and WAGASCI will start the neutrino beam measurement with full setup at May 2019. Until the neutrino beam measurement, the DAQ system of SideMRD will be integrated with WAGASCI and confirmed that it will not affect on the original DAQ system. Track matching method between WAGASCI and SideMRD will be developed.

References

[1] Y. Fukuda et al. (Super-Kamiokande Collaboration), Phys. Rev. Lett. 81, 1562 (1998).

[2] Z. Maki, M. Nakagawa and S. Sakata, Prog. Theor. Phys. 28, 870 (1962) .

[3] K.A. Olive et al. (PDG), Chin. Phys. C38, 090001 (2014).

[4] Yoshinari Hayato, Seminar of neutrino interaction with nucleus and their simulation, http://www-he.scphys.kyoto-u.ac.jp/nufrontier/files/hayato-20140111.pdf

[5] K.Abe et al. (T2K collaboration), Phys. Rev. D, 96, 092006 (2017).

[6] C. Patrignani et al. (Particle Data Group), Chin. Phys. C, 40, 100001 (2016) and 2017 update.

[7] I. Esteban et al., JHEP 1701, 087 (2017).

[8] K. Abe et al. (T2K Collaboration), Nucl. Instrum. Meth. A 659, 106 (2011).

[9] J-PARC TDR, KEK-Report 2002-13 and JAERI-Tech 2003-044, http://hadron.kek.jp/accelerator/TDA/tdr2003/index2.html (2003).

[10] K. Suzuki et al. Prog. Theor. Exp. Phys. 053C01 (2015).

[11] K. Abe et al. (T2K Collaboration), Nucl. Instrum. Methods Phys. Res. Sect. A 694, 211 (2012).

[12] Y. Fukuda et al. (Super-Kamiokande Collaboration), Nucl. Instrum. Meth. A 501, 418 (2003).

[13] K. Abe et al. (T2K Collaboration), Phys. Rev. D 88, no. 3, 032002 (2013).

[14] M. Antonova et al., Baby MIND Experiment Construction Status, arXiv:1704.08917, NUPHYS2016-PARSA, FERMILAB-CONF-17-205-APC (2016).

[15] 岡本浩大, J-PARC T59 実験 (WAGASCI) の横方向ミューオン検出器用シンチレータの性能評価, Bachelor's thesis, Yokohama National University (2018).

[16] Omega, SPIROC 2 User Guide (2009).

[17] F. Gastaldi, R. Cornat, F. Magniette, and V. Boudry, A scalable gigabit data acquisition system for calorimeters for linear collider, in proceedings of TIPP2014, PoS 193 (2014).

[18] N. Chikuma, Research and development of magnetized muon range detector and

readout electronics for a neutrino cross section experiment, Mather' s thesis, the University of Tokyo (2016).

[19] R. Tamura, Construction and performance of a neutrino detector for neutrino-nucleus interaction cross-section measurements, Master's thesis, University of Tokyo (2016).

[20] T. Koga, Research and development of a new neutrino detector for precise measurement of neutrino-nucleus cross sections, Master' s thesis, University of Tokyo (2015).